

Recent ground thermo-hydrological changes in a Tibetan endorheic catchment and implications for lake level changes

Léo C.P. Martin^{1,2,3}, Sebastian Westermann^{2,3,4}, Michele Magni¹, Fanny Brun^{1,4,5}, Joel Fiddes⁵Fiddes⁶, Yanbin Lei^{6,7}Lei^{7,8}, Philip Kraaijenbrink¹, Tamara Mathys⁸Mathys⁹, Moritz Langer^{9,10}Langer^{10,11}, Simon Allen¹¹Allen¹² and Walter W. Immerzeel¹

1. Faculty of Geosciences, Utrecht University, Utrecht, The Netherlands
2. Department of Geosciences, University of Oslo, Blindern, 0316 Oslo, Norway
3. [Aix Marseille Univ, CNRS, IRD, INRAE, CEREGE, Aix-en-Provence, France](#)
- 3,4. Center for Biogeochemistry in the Anthropocene, Oslo, Norway
- 4,5. Université Grenoble Alpes, CNRS, IRD, Grenoble INP, IGE, Grenoble, France
- 5,6. WSL Institute for Snow and Avalanche Research SLF, Davos, Switzerland
- 6,7. Key Laboratory of Tibetan Environment Changes and Land Surface Processes, Institute of Tibetan Plateau Research, Chinese Academy of Sciences, Beijing 100101, China
- 7,8. CAS Center for Excellence in Tibetan Plateau Earth System Sciences, Beijing 100101, China
- 8,9. Department of Geosciences, University of Fribourg, Fribourg, Switzerland
- 9,10. Alfred Wegener Institute Helmholtz Centre for Polar and Marine Research, 14473 Potsdam, Germany
- 10,11. Department of Geography, Humboldt Universität zu Berlin, 12489 Berlin, Germany
- 11,12. Department of Geography, University of Zurich, Zürich, Switzerland

Correspondence to: Léo Martin (leo.doug.martin@gmail.com)
Walter Immerzeel (w.w.immerzeel@uu.nl)

Abstract: [393401](#) words
Main: [11,14512,426](#) words, [1011](#) figures, 1 table
Appendices: [515441](#) words, [53](#) figures, 1 table

1 Abstract

2 Climate change modifies the water and energy fluxes between the atmosphere and the surface in
3 mountainous regions. This is particularly true over the Qinghai-Tibet Plateau (QTP), a major headwater
4 region of the world, which has shown substantial hydrological changes over the last decades. Among them,
5 the rapid lake level variations observed throughout the plateau remain puzzling, and much is still to be
6 understood regarding the spatial distribution of lake level trends (increase/decrease) and paces. The ground
7 across the QTP hosts either permafrost or seasonally frozen ground and both are affected by climate change.
8 In this environment, the ground thermal regime influences liquid water availability, evaporation and runoff.
9 Therefore, climate-driven modifications of the ground thermal regime may contribute to lake level
10 variations. For now, this hypothesis has been overlooked by modelers because of the scarcity of field data
11 and the difficulty to account for the spatial variability of the climate and its influence on the ground thermo-
12 hydrological regime in a numerical framework.

13 This study focuses on the cryo-hydrology of the catchment of Lake Paiku (Southern Tibet) for the 1980-
14 2019 period. We use TopoSCALE and TopoSUB to downscale ERA5 data and capture the spatial variability
15 of the climate in our forcing data. We use a distributed setup of the CryoGrid community model (version
16 1.0) to quantify thermo-hydrological changes in the ground during the period. Forcing data and simulation
17 outputs are validated with weather station data, surface temperature logger data and ~~the~~ lake level variations.
18 We show that both seasonal frozen ground and permafrost have warmed (~~1.70.17~~ °C per ~~century~~decade 2
19 m deep), increasing the availability of liquid water in the ground and the duration of seasonal thaw.
20 ~~Both~~Correlations with annual values suggest that both phenomena promote evaporation and runoff ~~but~~. Yet,
21 ground warming drives a strong increase in subsurface runoff, so that the runoff/(evaporation + runoff) ratio
22 increases over time. Summer evaporation is an important energy sink and we find active layer deepening
23 only where evaporation is limited. The presence of permafrost is found to promote evaporation at the expense
24 of runoff, consistent with recent studies. ~~Yet~~However, this relationship seems to be climate dependent and
25 we show that a colder and wetter climate produces the opposite effect. This ambivalent influence of
26 permafrost may help to understand the contrasting lake level variations observed between the south and north
27 of the QTP, opening new perspectives for future investigations.

28 Main text

29 1. Introduction

30 Climate change is amplified in mountainous environments, with major consequences for
31 ecosystems, landscapes, hydrology, human communities and infrastructure (IPCC, 2019). Station
32 observations show that global warming is elevation dependent, with the strongest warming rates being
33 observed at high elevationelevations (Pepin et al., 2015; Wang et al., 2014). Over the Qinghai-Tibet
34 Plateau (QTP), a significant increase in surface air temperatures has been recorded since the 1980s ~~(~~ in
35 particular in the North of the plateau ~~,~~ (Zhang et al., 2022 and references therein). It is accompanied by
36 a decrease in wind speed, ~~a humidification of the air, and a general increase in precipitation, but with a~~
37 ~~strong spatial variability~~ humidification of the air, and a general increase in precipitation, but with a
38 strong spatial variability (Bibi et al., 2018). Altogether, these changes have affected the surface energy
39 balance of the plateau through a shift of the Bowen ratio towards more latent heat fluxes, limiting the
40 sensible surface warming (Yang et al., 2014a). ~~Altogether, these changes have affected the surface~~
41 ~~energy balance of the plateau through a shift of the Bowen ratio towards more latent heat fluxes, limiting~~
42 ~~the sensible surface warming (Bibi et al., 2018; Yang et al., 2014 and references therein).~~

43 These changes in water and energy fluxes between the atmosphere and the surface have the potential
44 to alter the hydrological cycle of the QTP, which is the headwater region for major Asian rivers. As
45 such, increasing trends of evaporation over land have been measured (3.8 mm per decade since the
46 1960s) with strong spatial variability both in absolute values and increase rates (Wang et al., 2020b).
47 Changes in the seasonality of river discharge (Cao et al., 2006) and groundwater discharge (Niu et al.,
48 2011) were reported for the same period. Overall glacier shrinkage is also observed since the 1960s
49 with a persistent increase in glacier mass loss rates (Bhattacharya et al., 2021).

50 The QTP also features more than 1,000 lakes larger than 1 km² (Zhang et al., 2017), most of them
51 located in endorheic catchments. Lake volume changes are therefore attributable to climatic and
52 hydrological changes occurring within the lake catchment, such as glacier melt, ground ice melt,
53 precipitation, evaporation or runoff patterns. A majority of these lakes have experienced a pronounced

54 increase in water levels since the 1990s (Lei et al., 2013, 2014), a trend that was suggested to be mainly
55 driven by changes in precipitation and evaporation patterns (Yao et al., 2018) rather than by an increase
56 in glacier mass loss (Brun et al., 2020). Nevertheless, lake level variations are not uniform across the
57 QTP and exhibit important spatial variability. Whereas the northern and central QTP have recorded lake
58 expansion, the southern parts of the plateau have experienced lake shrinkage (Qiao et al., 2019; Zhang
59 et al., 2020, 2021a). Such a complex pattern challenges our understanding of the hydrological changes
60 occurring in these high Asian watersheds.

61 In this regard, new insights on hydroclimatic changes over the QTP can emerge from the
62 investigation of the coupled energy and water fluxes between the ground surface/subsurface and the
63 atmospheric boundary layer. These fluxes are driven by the climate and have a major impact on cold-
64 region hydrology (Bring et al., 2016; Gao et al., 2021; Pomeroy et al., 2007). Indeed, hydrological
65 variables (precipitation, evaporation, runoff) affect the soil water content, which changes its thermal
66 properties, the distribution between latent and sensible fluxes and thus substantially influences the
67 ground thermal regime ([Bring et al., 2016](#); [Koren et al., 1999](#); [Martin et al., 2019](#))([Bring et al., 2016](#);
68 [Koren et al., 1999](#); [Martin et al., 2019](#)). In turn, the ground thermal regime modifies the relative
69 proportion of frozen and liquid subsurface water, influencing infiltration possibilities and the amount
70 of water available for evaporation and surface/subsurface runoff (Carey and Woo, 2001; Yi et al., 2006).
71 So far, climate induced thermo-hydrological changes over the QTP have received limited attention.
72 Large-scale modeling studies reported changes in the seasonal ground freezing cycles characterized by
73 a reduction of the frost depth and duration of the frozen period since the 1960s (Qin et al., 2018; Wang
74 et al., 2020a) and notable ground warming trends in summer and winter (Qin et al., 2021). [Additionally,](#)
75 [ground warming over the QTP was reported to promote evaporation and to decrease runoff](#)Similar
76 [ground warming trends were reported in the regional modeling study from Qin et al. \(2017\), along with](#)
77 [an increasing trend in evaporation and a decrease of the runoff coefficient over time. Plateau-scale](#)
78 [surface energy balance modeling from](#) ([Qin et al., 2017](#); [Wang et al., 2020b](#)).[Wang et al. \(2020b\)](#)
79 [reported that increasing trends in evapotranspiration could be mainly explained by variations in air](#)
80 [temperature and net radiation at the surface.](#)

81 Complementary to seasonally frozen ground, permafrost is also a distinctive feature of climate-
82 surface interactions in cold regions. Large-scale permafrost modeling suggests that it covers a
83 significant part of the QTP, mainly as continuous permafrost in the north of the plateau and as
84 discontinuous or sporadic in the south (Obu et al., 2019). Permafrost on the QTP ~~has~~ usually has a low
85 ice content due to limited precipitation and strong evaporation (Wu et al., 2005; Yang et al., 2010).
86 Borehole temperature measurements show that it is a relatively warm type of permafrost (Biskaborn et
87 al., 2019; Wu and Zhang, 2008) and its exposure to high solar radiations makes it sensitive to changes
88 in surface conditions and climate change (Yang et al., 2010). Since the 1960s, climate change has driven
89 ~~the warming of~~ permafrost warming across the plateau (Ran et al., 2018; Shaoling et al., 2000). Ran et
90 al. (2018) ~~reports~~ report that most of the plateau ~~exhibit~~ exhibits a warming trend of the ground
91 comprised between ~~2.6~~ 0.26 and ~~7.4~~ 0.74 °C per ~~century~~ decade and half of the plateau warms at a rate
92 higher than 0.5 °C per ~~century~~ decade. This warming is accompanied by upward migration (of around
93 100 m between the 1960s and 2000s) and shrinkage of permafrost covered areas (24% of ~~the~~ permafrost
94 extent lost between the 1960s and ~~the~~ 2000s, Ran et al., 2018).

95 Permafrost grounds are characterized by a strong interplay between the ground thermal regime and
96 the land hydrology. Seasonal thawing and freezing of the active layer ~~is~~ are driven by the surface energy
97 balance and, in return, influences surface and subsurface runoff (Kurylyk et al., 2014; Sjöberg et al.,
98 2021; Walvoord and Kurylyk, 2016) and evaporation (Gao et al., 2021). In this regard, both large-scale
99 and regional modeling ~~indicates~~ indicate that thawing permafrost enhances evapotranspiration (Qin et
100 al., 2017; Wang et al., 2020b). Qin et al. (2017) also ~~reports~~ report that the increase in evaporation is
101 logically concomitant with a decrease in ~~the~~ runoff coefficient. Additionally, permafrost stores water as
102 ground ice and its thawing can trigger the release of liquid water in the watershed, contributing up to
103 15% of the ~~yearly~~ annual river streamflow (Cheng and Jin, 2013; Yang et al., 2019).

104 The aforementioned hydrological changes are tied to various interdependent climate-driven
105 physical processes happening at the ground surface and subsurface (e.g. surface energy balance,
106 infiltration, water phase change, heat conduction...). Because these processes exhibit a strong spatial
107 variability in high mountain environments, ~~they are~~ it is challenging to represent ~~them~~ them accurately
108 together on large spatial scales. Therefore, a deeper understanding of the impact of ground thermo-

109 hydrological changes on the High Asia water cycle can be gained through small-scale physical modeling
110 of these processes. Yet, for now, physics-based approaches at the catchment scale aiming to connect
111 the ground thermo-hydrological regime and the observed hydrological changes on the QTP (such as
112 lake level changes) remain scarce. They are however a powerful approach to tackle the question: how
113 much climate-driven ground thermal changes might affect the water cycle in high mountain headwater
114 regions? In this study, we use physical land surface modeling to quantify the ground thermo-
115 hydrological changes [ofin](#) an endorheic Tibetan catchment over the last 40 years as a response to climate
116 change. We show the interplay in the water and energy fluxes occurring between the atmosphere, the
117 surface and the subsurface and discuss their impact on the hydrology of the catchment and their
118 implication regarding lake level variations.

2. Study area: the Paiku catchment

The Paiku catchment is located in south-western Tibet, China, close to the border with Nepal (28.8°N—85.6°E, Fig. 1). Its southern edge lies 7 km from the Shishapangma peak (8027 masl). The catchment is endorheic and spans over 78 km from North to South, 66 km from East to West and covers 2 400 km². The median elevation of the catchment is 4872 masl, ranging from 7272 masl to its lowest point, the lake Paiku at 4580 masl. Geologically, the catchment is mainly located in the Tethys Himalayan, and thus, an important part of the formations underlying the catchment are metamorphized sedimentary series. The southern part of the catchment crosses the Southern Tibetan Detachment, and thus, the southern ridges of the massif belong to the High Himalayan metamorphic formations in the west and to the High Himalayan leucogranites of the Shishapangma massif on the east. The north and north-east ridges are formed by granite intrusions surrounded by metamorphic domes. The inner part of the catchment presents Plio-Quaternary formations such as alluvial fans close to the ridges and inclined alluvial plains in its inner parts (Fig. B of the appendices, Aoya et al., 2005; Searle et al., 1997; Wünnemann et al., 2015).

2. Automatic Weather Station (AWS) observations (5033 masl, Oct 2019—Sept 2021, Fig. 1) show that the climate in the catchment is characterized by a relatively small temperature amplitude during the year (around 20 °C, JJA being the warmest months and DJF the coldest) and significant daily amplitude (up to 10 °C during the warm season). The mean annual temperature is -1.5 °C at the AWS, where night freezing can occur until the beginning of June and

restart Study area: the Paiku catchment

The Paiku catchment is located in south-western Tibet, China, close to the border with Nepal (28.8°N - 85.6°E, Fig. 1). Its southern edge lies 7 km from the Shishapangma peak (8027 masl). The catchment is endorheic and spans over 78 km from North to South, 66 km from East to West and covers 2 400 km². The median elevation of the catchment is 4872 masl, ranging from 7272 masl to its lowest point, lake Paiku at 4580 masl. Geologically, the catchment is mainly located in the Tethys Himalayan,

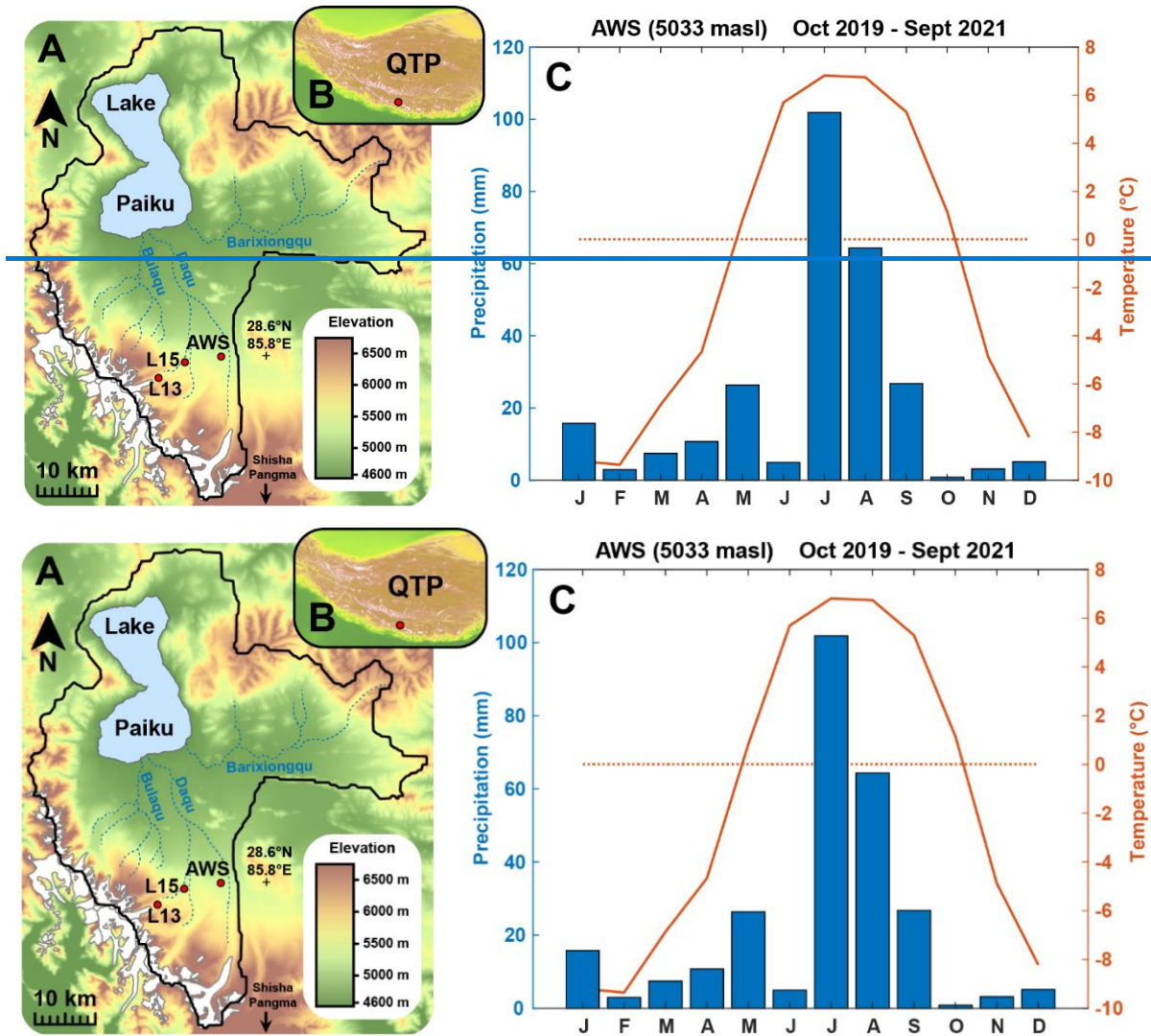
144 [and thus, an important part of the formations underlying the catchment are metamorphized sedimentary](#)
145 [series. The southern part of the catchment crosses the Southern Tibetan Detachment, and thus, the](#)
146 [southern ridges of the massif belong to the High Himalayan metamorphic formations in the west and to](#)
147 [the High Himalayan leucogranites of the Shishapangma massif on the east. The north and north-east](#)
148 [ridges are formed by granite intrusions surrounded by metamorphic domes. The inner part of the](#)
149 [catchment presents Plio-Quaternary formations such as alluvial fans close to the ridges and inclined](#)
150 [alluvial plains in its inner parts \(Appendix B, Fig. B0, Aoya et al., 2005; Searle et al., 1997; Wünnemann](#)
151 [et al., 2015\).](#)

152 [Automatic Weather Station \(AWS\) observations \(5033 masl, Oct 2019 – Sept 2021, Fig. 1\) show](#)
153 [that the climate in the catchment is characterized by a relatively small temperature amplitude during the](#)
154 [year \(around 20 °C, JJA being the warmest months and DJF the coldest\) and significant daily amplitude](#)
155 [\(up to 10 °C during the warm season\). The mean annual temperature is -1.5 °C at the AWS, where night](#)
156 [freezing can occur until the beginning of June and resume](#) at the beginning of October. The catchment
157 is dry (\sim (200-300 mm year⁻¹) and precipitation mostly [fallfalls](#) as rain during the monsoon (JJAS).

158 Around 5% of the catchment is covered by glaciers (RGI Consortium, 2017), which are
159 concentrated in its southwestern part. They feed several proglacial lakes that can reach up to 6 km in
160 length. Geodetic glacier mass budgets show that, similar to other glaciers in the region, glaciers of the
161 Paiku catchment have undergone sustained mass loss at least since the 1970s, with an average mass
162 balance of -0.3 m w.e.a⁻¹ until the beginning of the 2000s and around -0.4 m w.e.a⁻¹ [afterwardsthereafter](#)
163 (Bhattacharya et al., 2021). There are more than 10 rivers that drain the catchment towards the lake and
164 most of them only exhibit a seasonal activity during the monsoon months. The three main ones are
165 (Fig.-1), Daqu (glacier-fed, 450 km²), Bulaqu (glacier-fed, 325 km²) and Barixiongqu (non-glacier-fed,
166 703 km²) (Lei et al., 2018).

167 In the north-west of the catchment, Lake Paiku covers approx. 280 km² (11.5% of the catchment
168 surface area) and spans over 27 km from north to south. It has a mean water depth of 41 m, with a
169 maximum water depth of 73 m (Lei et al., 2018). It receives water from direct precipitation and from
170 land and glacier runoff which can be routed at the surface via the river systems or the subsurface via
171 the alluvial formations. Because it is hydrologically closed, the lake mainly loses water through

172 evaporation. Previous studies reported lake level fluctuations over different time scales. It reached 4665
173 masl (85 m higher than [the](#) present level) prior to 25 ka BP and at the onset of the Holocene (11.9-9.5
174 ka BP). Afterwards, the lake shrank gradually (Wünnemann et al., 2015). More recently, the lake level
175 decreased by 3.7 m between 1972 and 2015, losing 4.2% of its surface and 8.5% of its volume ([Fig. 2,](#)
176 [Lei et al., 2018](#)). At the seasonal scale, the lake level cycle has an amplitude of ~ 0.4 m. It is marked
177 by a strong increase during the monsoon period (JJAS) supported by direct precipitation, glacier melt
178 and land runoff. From October and until the next monsoon period, evaporation dominates the lake mass
179 budget and the level decreases rapidly until January and at a slower rate afterwards (Lei et al., 2021).



180

181

182

183

184

185

186

187

Figure 1. The Paiku Catchment. A: Topographic and hydrologic map of the catchment with the glaciers in white, the ephemeral rivers in dark blue and the lake in light blue- (elevation: SRTM data courtesy of the U.S. Geological Survey). AWS: Automatic Weather Station. L13 and L15 are surface temperature loggers (Sect. 3.1). B: Localization of the catchment over the QTP. C: Monthly temperature and precipitation recorded at the AWS between October 2019 and September 2021.

188 3. Material and methods

189 3.1. Field measurements

190 An AWS was set up in October 2019 in the South of the catchment at an elevation of 5033 masl
191 (Fig. 1). It is equipped with various sensors which record air temperature, pressure, relative humidity,
192 wind speed, incoming and outgoing long and short wave radiations and precipitation every 15 minutes.
193 The meteorological record extends to September 2021 and covers a period of nearly 2 years. We used
194 it to evaluate and correct the distributed downscaled climatic forcing we ~~used~~rely on in our modeling
195 framework (Sect. 3.2.52.).

196 Two temperature loggers recorded the surface temperature in the vicinity of the AWS location.
197 Logger 15 (L15) is located at 5055 masl, 6 km west ~~from~~of the AWS. Logger 13 (L13) is located at
198 5356 masl, 12 km west ~~from~~of the AWS (Fig. 1). Both loggers were buried 10 to 15 cm below the
199 surface to avoid direct solar radiation on the sensors and recorded surface temperature at a 20-~~minutes~~
200 ~~time step~~minute timestep from October 2017 to October 2018. These surface temperature records were
201 used to evaluate the simulations (Sect. 3.2.54.).

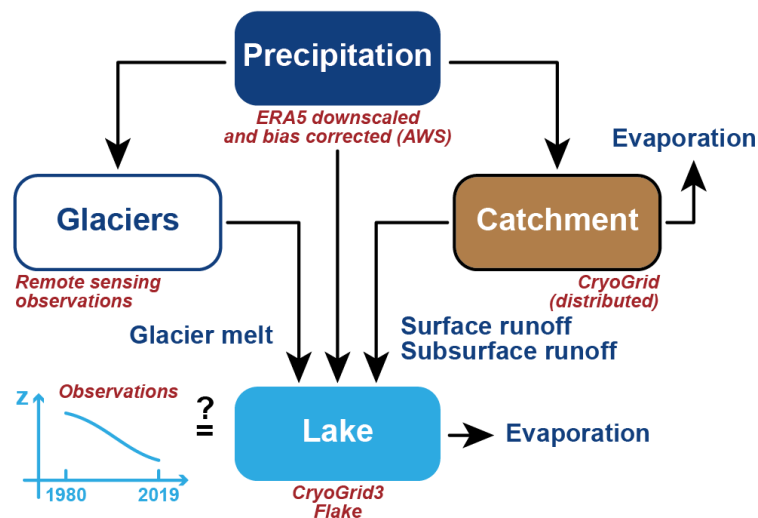
202 3.2. Catchment thermo-hydrological modeling

203 3.2.1. Conceptual hydrological model for the catchment

204 ~~In order to~~To understand the level variations of lake Paiku over the last 40 years (1980-2019
205 period), we develop an approach at the catchment scale. Because the catchment is hydrologically closed,
206 the lake receives water input via direct precipitation, land surface and subsurface runoff ~~and glacier~~
207 ~~runoff. Conversely, it only loses mass via evaporation. As such, the present study requires quantification~~
208 ~~of all these terms of the hydrological balance., and glacier runoff. Conversely, it loses mass via~~
209 ~~evaporation. Because the quantification of water flows between the lake and potential aquifers~~
210 ~~surrounding it is difficult (Rosenberry et al., 2015), our approach assumes that these flows are~~
211 ~~negligible. The present study requires quantification of the different terms of the hydrological balance.~~
212 Under these assumptions, the hydrological balance of the lake is given by the following equation:

$$213 \Delta Z_{\text{Lake}} = \text{Precipitation}_{\text{Lake}} + \text{Runoff}_{\text{Land}} + \text{Runoff}_{\text{Glacier}} - \text{Evaporation}_{\text{Lake}}$$

214 The production of forcing data for the catchment (including precipitation) is detailed in Sect. 3.2.2.
 215 The land hydrology processes are quantified using the CryoGrid community model (version 1.0)
 216 (Westermann et al., 2022) as described in section 3.2.3. Distributed 1D simulations are used to quantify
 217 land evaporation and runoff. The routing of water in the catchment is not represented and the runoff
 218 computed for a given simulation is directly accounted as a water input for the lake. The evaporation
 219 from the lake is simulated using the CryoGrid3-Flake model (Langer et al., 2016) as described in
 220 Section 3.2.45. Glacier melt is not modeled, but estimated for the study period (1980-2019) from remote
 221 sensing observations. From these observations, [glaciersglacier](#) yield is calculated as described in Sect.
 222 3.2.6. Our catchment-scale approach to represent the hydrological balance of the lake is summarized in
 223 Fig.-2.



224
 225 *Figure 2. Conceptual hydrological framework for the study.*
 226

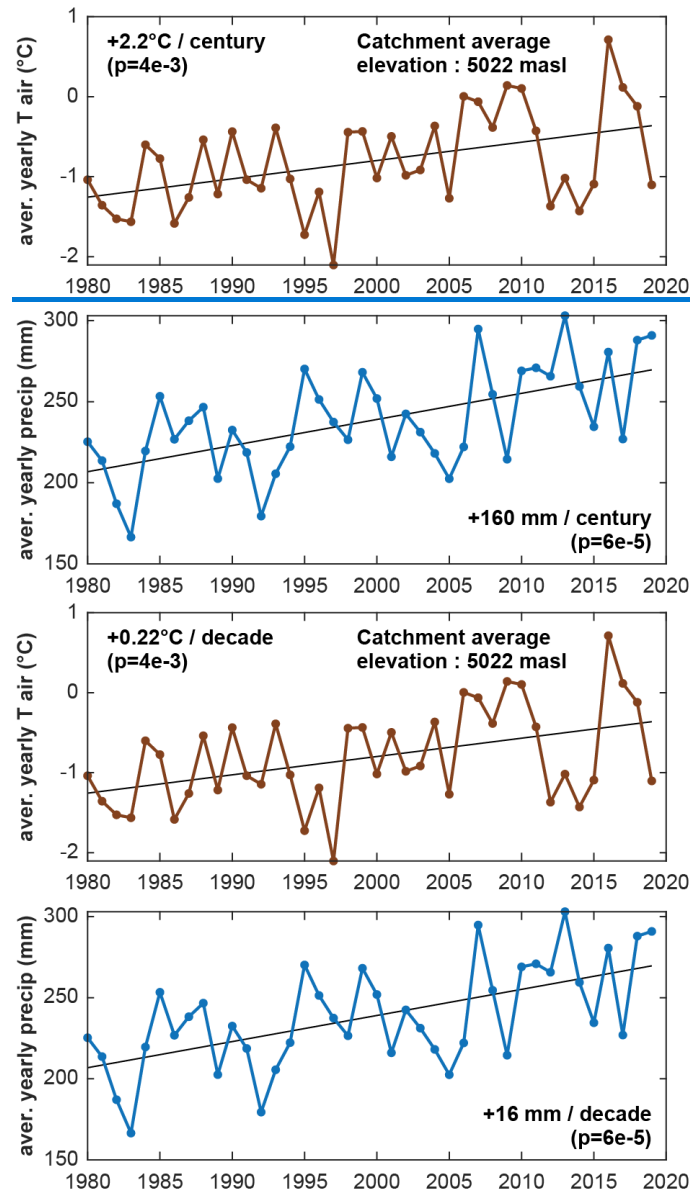
227 **3.2.2. Forcing data production and validation**

228 In high mountain environments, topography creates strong spatial variability of temperature and
 229 incoming radiation, which impact the surface energy balance (Klok and Oerlemans, 2002) and the
 230 ground thermo-hydrological regime (Magnin et al., 2017). Our approach requires forcing data that (i)
 231 captures this variability, (ii) includes numerous variables such as air temperature, incoming long and
 232 short wave radiations, wind speed, specific humidity, rain and snowfall and (iii) [eovercovers](#) the 40
 233 years study period at a sub-daily timestep. The TopoSCALE approach (Fiddes and Gruber, 2014) was
 234 developed for this purpose and allows to downscale reanalysis products like ERA5 (Hersbach et al.,
 235 2020) at high resolution (here $\sim 100 \times 100$ m). Additionally, because working at a 10^{-2} km² spatial

236 resolution over a 2400 km² catchment would require more than 200,000 forcing files and simulations,
237 we rely on the TopoSUB method (Fiddes and Gruber, 2012) to reduce computational costs. This method
238 uses a SRTM30 Digital Elevation Model to explore redundancies in physiographic parameters of the
239 study area such as elevation, aspect, slope and sky-view factor and [to](#) identify groups of high-resolution
240 pixels (100 x 100 m) sharing similar values for these parameters. From there, all the high-resolution
241 pixels belonging to such a group are only described as a single TopoSUB point, for which climatic
242 variables can be downscaled to create one single dataset of climatic timeseries. The degree of similarity
243 required by TopoSUB to identify groups of high-resolution pixels with redundant physiographic
244 parameters can be adjusted by choosing the final number of TopoSUB points (and thus climate datasets)
245 that should be used to cover the area corresponding to one ERA5 pixel. The Paiku catchment intersects
246 8 ERA5 pixels at 30 km resolution and we chose to use 50 TopoSUB points within each ERA5
247 [pixelspixel](#) to cover the spatial variability created by the topography on small-scale climate. Ultimately,
248 368 TopoSUB points are used to cover the catchment. The average level of redundancy (i.e. the average
249 number of high-resolution pixels represented by a single TopoSUB point) is 723 ± 745 (1σ , median:
250 506, min: 1, max: 4347). [Appendix C](#), Fig. [C0](#) shows the distribution of the TopoSUB points and a
251 reconstruction of the topography of the catchment based on this approach. The period covered by the
252 forcing datasets starts on 1st January 1980 and ends on 31st August 2020 (40 years and 8 months).

253 In the TopoSCALE statistical downscaling approach, we do not rely on the AWS data and thus the
254 downscaled ERA5 data can be biased, as is often the case over Asia (Jiang et al., 2020, 2021; Jiao et
255 al., 2021; Orsolini et al., 2019). Comparison against the available AWS observations ([Appendix D](#), Fig.
256 [D0](#)) indeed highlights notable differences in variables such as air temperature and precipitation. From
257 these differences, we derived monthly bias correction factors that we [applyapplied](#) systematically to all
258 of the 368 climate forcing datasets. The catchment-averages for precipitation and air temperatures are
259 shown in Fig. [3](#).

260 [3. In this figure and across the rest of the study, we use p-values to evaluate the significance of linear](#)
 261 [trends in the temporal evolution of certain variables \(temperature, precipitation, evaporation...\).](#) This
 262 [p-value tests the null hypothesis which supposes that the value of the slope is equal to zero. The](#)
 263 [hypothesis is tested using the Student's t-test, by comparing the distance between the estimated slope](#)
 264 [and 0, relative to the standard error of the slope. We did not report trends when this p-value \(probability](#)
 265 [of a null slope\) was higher than \$5 \cdot 10^{-3}\$.](#)



266
 267
 268 *Figure 3. Climate forcing data for the land and lake modeling. Yearly Annual catchment-average air*
 269 *temperature (2 m above ground) and annual total precipitation for the study period. Note that the model*
 270 *is also forced by incoming short and long wave radiations, humidity, windspeed and air pressure.*
 271 *Details about the spatial and temporal resolution of the distributed forcing data are presented in <#>*
 272 *Sect. 3.2.2.*

273
 274 **3.2.3. The CryoGrid community model (version 1.0)**

275 To simulate the ground thermo-hydrological regime, we use the CryoGrid community model
276 (Westermann et al., 2022). The CryoGrid community model (CG) is a land surface model designed for
277 applications in cold regions where seasonal frozen ground or permafrost may occur. The model
278 implements heat transfer in a 1D soil column, accounting for freeze-thaw processes of soil water using
279 effective heat capacity (Nakano and Brown, 1972). To do so, soil freezing curves are based on
280 Dall’Amico et al. (2011) as detailed in Westermann et al. (2013). Vertical water movement in the soil
281 column is based on Richards equation (Richards, 1931; Richardson, 1922). The soil matric potential
282 and hydraulic conductivity follow van Genuchten (1980) and Mualem (1976). Additionally, to represent
283 the obstruction of connected porosity by ice formation, the hydraulic conductivity is reduced by a factor
284 dependent on the local ice content, following Dall’Amico et al. (2011). The model features the
285 snowpack module called *CG Crocus* described in Zweigel et al. (2021) that adapts the snow physics
286 parameterizations from the CROCUS scheme (Vionnet et al., 2012) to the native snow module of
287 CryoGrid3 (Westermann et al., 2016). At the surface, the model uses a surface energy balance module
288 to calculate the ground surface temperature and water content. The turbulent fluxes of sensible and
289 latent heat are calculated using a Monin–Obukhov approach (Monin and Obukhov, 1954). Evaporation
290 is derived from the latent heat fluxes using the latent heat of evaporation and is adjusted to the available
291 water in the soil ~~and the. It occurs in the first grid cell only, but~~ water ~~loss is distributed vertically~~ can
292 be drawn upwards due to ~~decreases exponentially with depth.~~

matric potential differences. Because vegetation is very scarce in the catchment, we do not expect transpiration to have a strong imprint on evapotranspiration and our calculations do not unravel evaporation from transpiration.

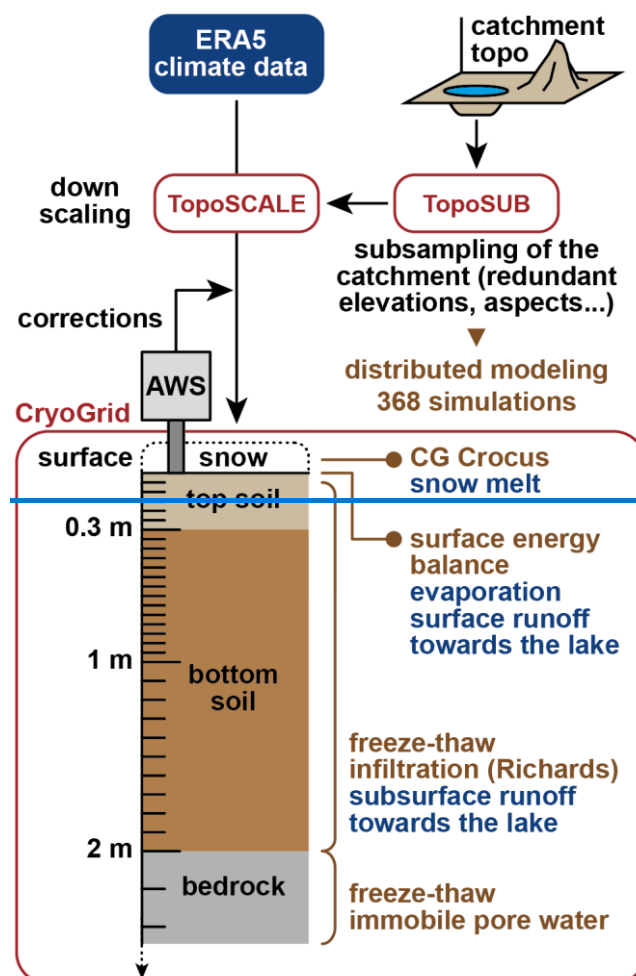
3.2.4. Model setup and validation

The setup of the CryoGrid community model for the land is presented in Fig. 4. To capture the high spatial variability of mountainous climate, our approach relies on the 368 climate forcing datasets to cover the catchment (see section 3.2.3). This approach enables us to perform spatially distributed modeling. All of the 368 simulations are independent and use the same parameterization. In absence of direct observation of the soil stratigraphy within the catchment, the soil column was designed to agree with field observations in the region (Hu et al., 2020; Luo et al., 2020; Wang et al., 2008, 2009; Yang et al., 2014b; Yuan et al., 2020), to be consistent with similar modeling approaches across Tibet (Chen et al., 2018; Song et al., 2020) and to be consistent with input datasets (Shangguan et al., 2013, 2017). Thus, the soil stratigraphy is divided ~~into~~ into 3 units: a top soil (0.3 m thick), a bottom soil (1.7 m thick), and a bedrock unit (extending beyond the depth of interest of the study). An overview of the parameters for each unit, their source and the way they are calculated is presented in Table Appendix A, Tab. A1. Regarding the processes implemented in the model (Sect. 3.2.3), infiltration according to Richards equation only occurs in the top and bottom soil units. The bedrock unit has a static water content. ~~Additionally, to simulate subsurface runoff towards the lake, the two soil units are hydrologically connected to a reservoir at the elevation of the lake. This reservoir drains excess water of the soil column when its water content exceeds field capacity. This drainage is quantified using Darcy's law and relies on a hydraulic slope taken as the mean slope of the catchment~~ Unraveling surface from subsurface flow is an ongoing challenge in catchment-scale hydrology (McDonnell, 2013) and this distinction is important in mountain terrains where these two flows can behave differently due to the complex topography (Gao et al., 2014; Seibert et al., 2003). For this study, we rely on a simple approach that computes surface and subsurface flow as follows.

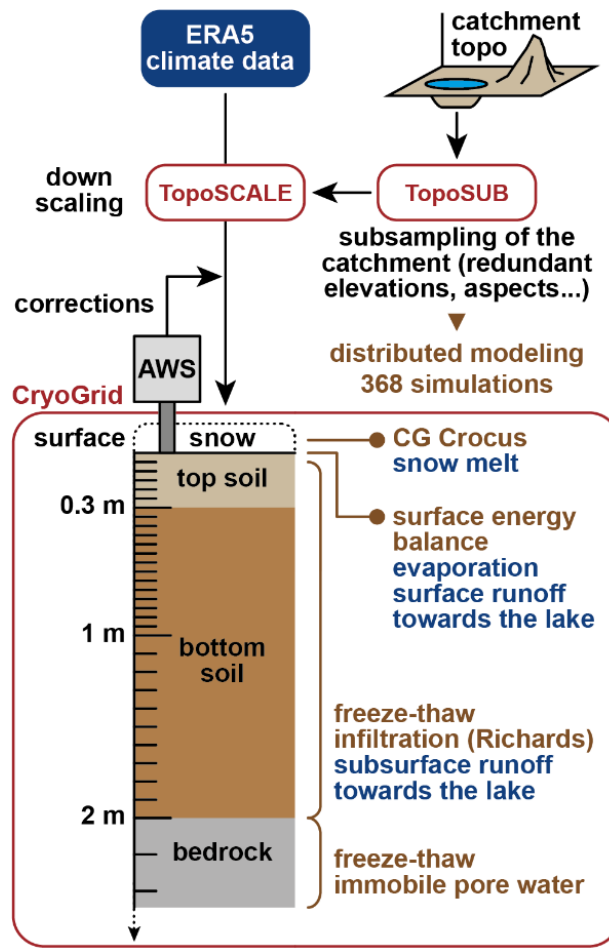
On the one hand, surface runoff is computed relative to the saturation level of the soil column. When the entire soil column is saturated ($WC = porosity$), additional water input from precipitation or snowmelt is directly counted as surface runoff. On the other hand, subsurface runoff is computed

321 [relative to the field capacity of the ground, which is an input parameter of the model. When the water](#)
 322 [content \(WC\) of a ground cell exceeds this field capacity \(FC\), the amount of water corresponding to](#)
 323 [WC-FC is available to produce subsurface runoff. We use the lateral boundary condition](#)
 324 [LAT_WATER_RESERVOIR from the CryoGrid community model \(Westermann et al., 2022\) to](#)
 325 [account for this subsurface runoff. The speed at which this available water exits the soil column towards](#)
 326 [the lake is calculated with Darcy's law, using the hydrological conductivity of the ground and the mean](#)
 327 [slope of the catchment as hydraulic slope.](#)

328 Because we do not have knowledge of the distributed thermal state with depth over the catchment
 329 at the beginning of the simulations, we assume temperature profiles were in equilibrium with the climate
 330 of the 5 first years of modeling (1980-1984). To do so, we start our simulations with a 60-years-year
 331 spin-up of these first 5 years (12 repetitions), which is sufficient to establish a stable temperature profile
 332 [#over the first 9 to 80 meters depending on the simulations, extending beyond](#) the hydrologically active
 333 part of the ground (the first 2 meters).



334



335

336 *Figure 4. Modeling framework for the land hydrology. ERA5 data are downscaled using the TopoSUB*
 337 *and TopoSCALE approaches (Fiddes and Gruber, 2012, 2014). The downscaled data are bias-*
 338 *corrected based on the AWS observations. Distributed 1D simulations are performed using the*
 339 *CryoGrid community model (Westermann et al., 2022). The vertical resolution is indicated with the tick*
 340 *marks on the depth axis.*

341

342 To validate model simulations, the simulated ground surface temperatures (GST) are compared to
 343 the two temperature logger time series acquired in the vicinity of the AWS (Sect. 3.1). We used this
 344 comparison to calibrate the surface roughness used for the surface energy balance calculations in the
 345 model.

346 [The following method is used to produce area-averaged evaporation and runoff \(in mm water](#)
 347 [equivalent\) in a zone of interest. For a given TopoSUB point in this zone, the model produces](#)
 348 [hydrological values in m³ using the area of a TopoSUB pixel on the catchment map. Then these values](#)
 349 [are multiplied by the number of pixels in the zone corresponding to this TopoSUB point in particular,](#)
 350 [and this for all the relevant TopoSUB points covering the zone \(e.g. evaporation in warm permafrost\).](#)
 351 [Then the area of interest is calculated by counting the number of pixels in the zone of interest and](#)

352 [multiplying this number by the area of a pixel. Then the total volume is divided by the total surface for](#)
353 [the zone of interest to obtain the final value in mm.](#)

354 3.2.5. *Lake modeling*

355 The lake thermo-hydrological response to the climatic forcing data is simulated using the
356 CryoGrid3-Flake model (Langer et al., 2016). The two models were coupled by Langer et al. (2016) to
357 simulate the thermal regime of thermokarst lakes (including surficial water freezing and melting) and
358 underlying ground. Here we use the coupled models mainly to quantify evaporation at the lake surface.
359 In the coupled model, the native surface energy balance module of CryoGrid3 (Westermann et al., 2016)
360 was amended to account for processes tied to free water surface energy balance: (i) the
361 ~~dependanc~~[dependence](#) of the albedo of a water surface to solar angle (and thus time of the day) and
362 wind speed (and wave formation), (ii) the ~~dependanc~~[dependence](#) of the surface roughness length to
363 wind speed (and wave formation) and (iii) the exponential decay of incoming radiation with depth in
364 the water column. ~~Similarly~~[Similar](#) to the land simulations, the lake simulations were forced by the
365 downscaled ERA5 data, [\(with the TopoSUB and TopoSCALE methodology\)](#), with the corrections
366 derived from the AWS data (Sect. 3.2.2). The simulations were initiated with a 20-~~years-year~~[year](#) spin-up
367 of the 1980-1984 climate. [The simulation results corresponding to the four ERA5 tiles covering the lake](#)
368 [were then averaged using the respective spatial footprint of each tile on the lake.](#)

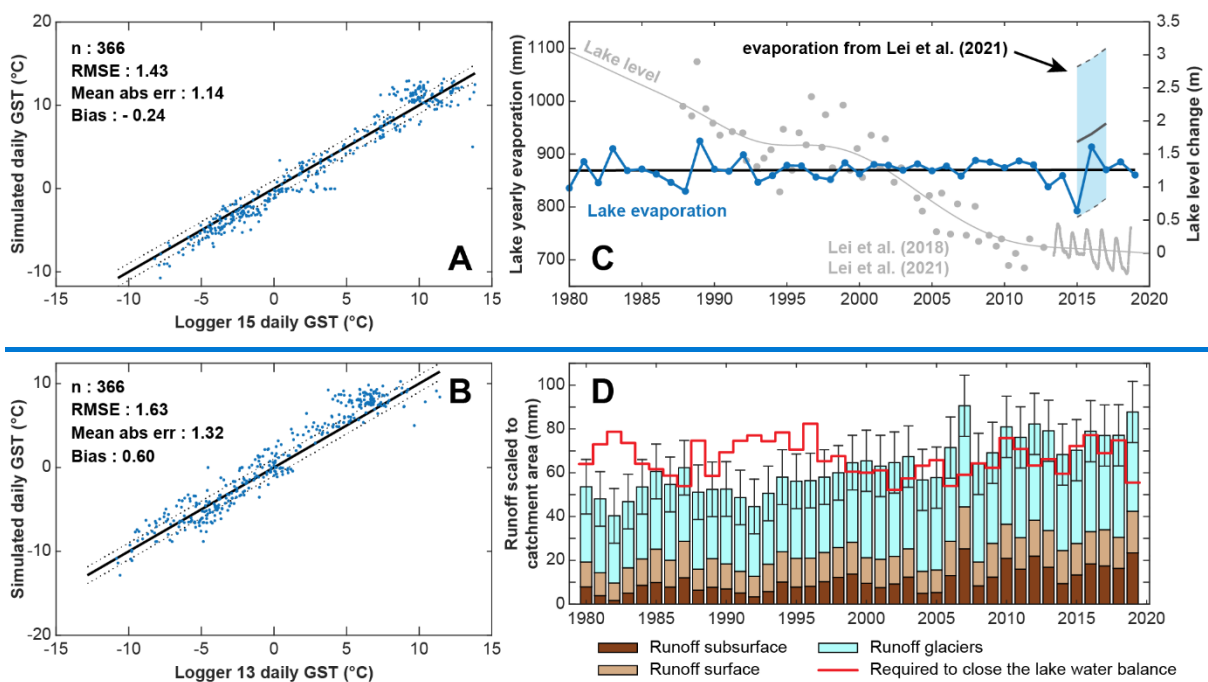
369 3.2.6. *Quantification of glacier mass change*

370 Multiple studies quantified the volume change of the glaciers located within [the](#) Paiku catchment
371 in the recent past (1970s to 2020). There are no field based measurements of glacier mass balance
372 available in this catchment to our knowledge. As a consequence, we rely solely on ~~the~~ geodetic mass
373 balance studies (Brun et al., 2017; Hugonnet et al., 2021; King et al., 2019; Maurer et al., 2019; Shean
374 et al., 2020). All these studies estimated glacier volume changes over periods of 20-30 years from
375 satellite derived DEMs. As a consequence, we can only estimate the average annual glacier mass
376 balance, and not the year to year variability. Glaciers occupy approximately 113 km² in the Paiku
377 catchment. They have shrunk for the past fifty years at a rate of 0.44 % y⁻¹, from an area of 132 km² in
378 1975 to 122 km² around 2000 and to their current extent (Bolch et al., 2019; King et al., 2019). The
379 average mass balances for the period 1975-2000 and 2000-2020 are $-3.9 \pm 2.1 \times 10^{10}$ kg y⁻¹ and $-5.4 \pm$
380 2.4×10^{10} kg y⁻¹, respectively ($-4.6 \pm 2.5 \cdot 10^7$ m³ and $-6.4 \pm 2.8 \cdot 10^7$ m³ with a 850 kg m⁻³ density). These
381 mass balances correspond to specific mass balances of -0.31 ± 0.17 m of water equivalent per year (w.e.
382 y⁻¹) and -0.47 ± 0.21 m w.e. y⁻¹, respectively.

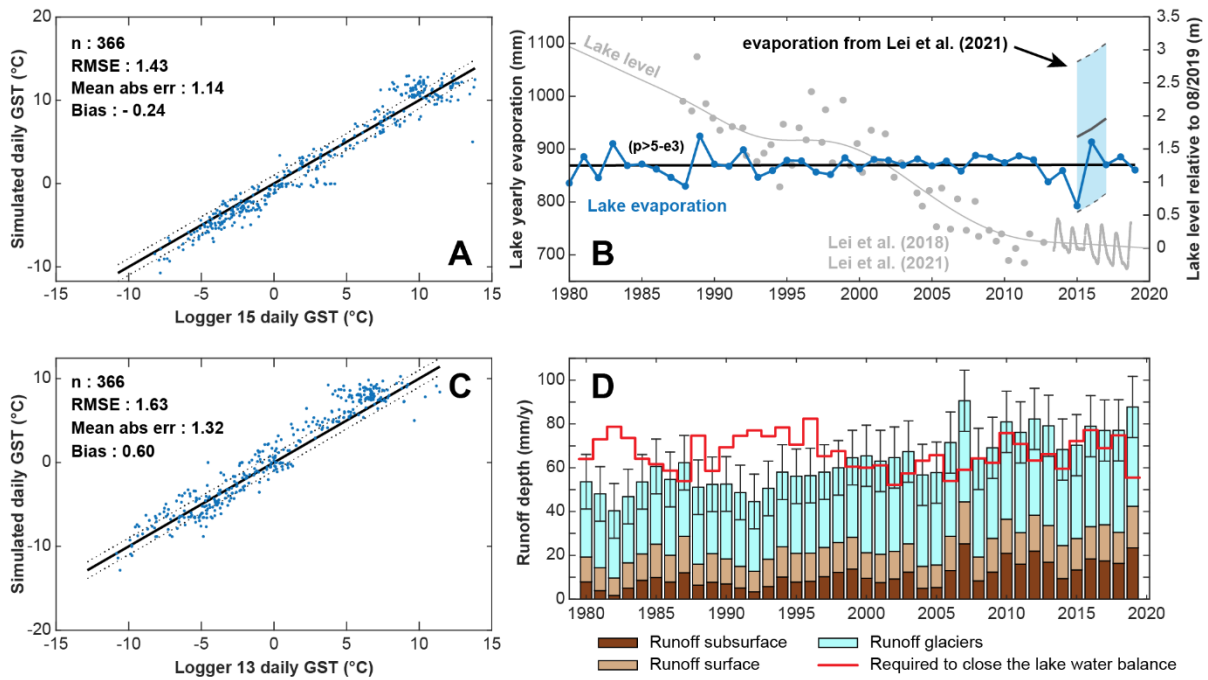
383 **4. Results**

384 **4.1. Model validation and lake evaporation**

385 [Model validation results are presented in Fig. 5.](#) Simulated daily ground surface temperatures are
386 in good agreement with the observed ones [with, showing](#) a bias of $-0.2\text{ }^{\circ}\text{C}$ and $0.6\text{ }^{\circ}\text{C}$ and a RMSE of
387 $1.4\text{ }^{\circ}\text{C}$ and $1.6\text{ }^{\circ}\text{C}$ for loggers 15 and 13, respectively (Fig. 5A and [5B5C](#)). Most of this RMSE is
388 explained by a mismatch between model and observations in the tails of the temperature distribution,
389 whereas intermediate temperatures exhibit the best agreement with observations.



390



391
 392 *Figure 5. Model validation. A and BC: modeled mean daily ground surface temperatures compared to*
 393 *measured ground surface temperatures for logger 15 and logger 13 (location on Fig. 1). CB: modeled*
 394 *yearly annual lake evaporation (blue curve) and comparison with values calculated by Lei et al. (2021)*
 395 *in the light blue zone. The greygray curve shows the smoothed lake level variations relative to August*
 396 *2019 based on observations from Lei et al. (2018) (greygray points) and Lei et al. (2021) (greygray*
 397 *oscillating line). D: Comparison between the runoffs required to reproduce the observed lake variations*
 398 *(red curve, derived from lake level, lake area, forcing data and lake evaporation) and the sum of the*
 399 *glacier and land runoff we derive from remote sensing observations and modeling respectively (Sect.*
 400 *3.2). Error bars are associated to the glacier values and come from the geodetic results. Runoff values*
 401 *are expressed as heights scaled to the land surface of the Paiku catchment.*

402
 403 Yearly Annual lake evaporation mainly ranges between 800 and 900 mm per year, (Fig. 5B), with
 404 a mean value of 870 ± 23 mm (1σ). Lake evaporation does not exhibit a linear trend of increase or
 405 decrease and is mostly dominated by year-to-year variability. Though slightly lower, our evaporation
 406 results are in agreement with the values from Lei et al. (2021), which are derived from local and regional
 407 meteorological observation and lake budget calculation (Fig. 5, CB). We used the simulated
 408 evaporation together with the lake level data and lake area data from Lei et al. (2018) and Lei et al.
 409 (2021) and the precipitation forcing datasets (3.2.2) to derive the total runoff (land + glacier) required
 410 as an input to the lake budget to reproduce the lake variations. This required runoff corresponds to the
 411 red line of Fig. 5D. The required runoff volumes are scaled to the land area of the catchment to be
 412 comparable with the other variables. The fact that these values are substantially higher than 0 mm per
 413 year highlights the importance of the land and glacier contribution to the lake budget.

414 Fig. 5D also presents the runoff values derived from the land cryo-hydrological modeling and from
415 the glacier remote sensing investigations. Annual volumes are expressed as mm over the land part of
416 the catchment (excluding the lake). ~~Based on the characteristics of remotely sensed observations~~As
417 ~~presented in section 3.2.6~~, glacier mass balance values are considered constant for the 1980-2000 period
418 and ~~the~~ 2000-2019 period and ~~are~~ respectively equal to $-4.6 \pm 2.5 \cdot 10^7$ and $-6.4 \pm 2.8 \cdot 10^7$ m³ per year.
419 The addition of ~~yearlyannual~~ precipitation to these values to quantify the total glacier runoff introduces
420 year-to-year variability to the glacier runoff. At the catchment scale, the average glacier runoff over
421 the 40 years is 39 ± 13 mm per year.

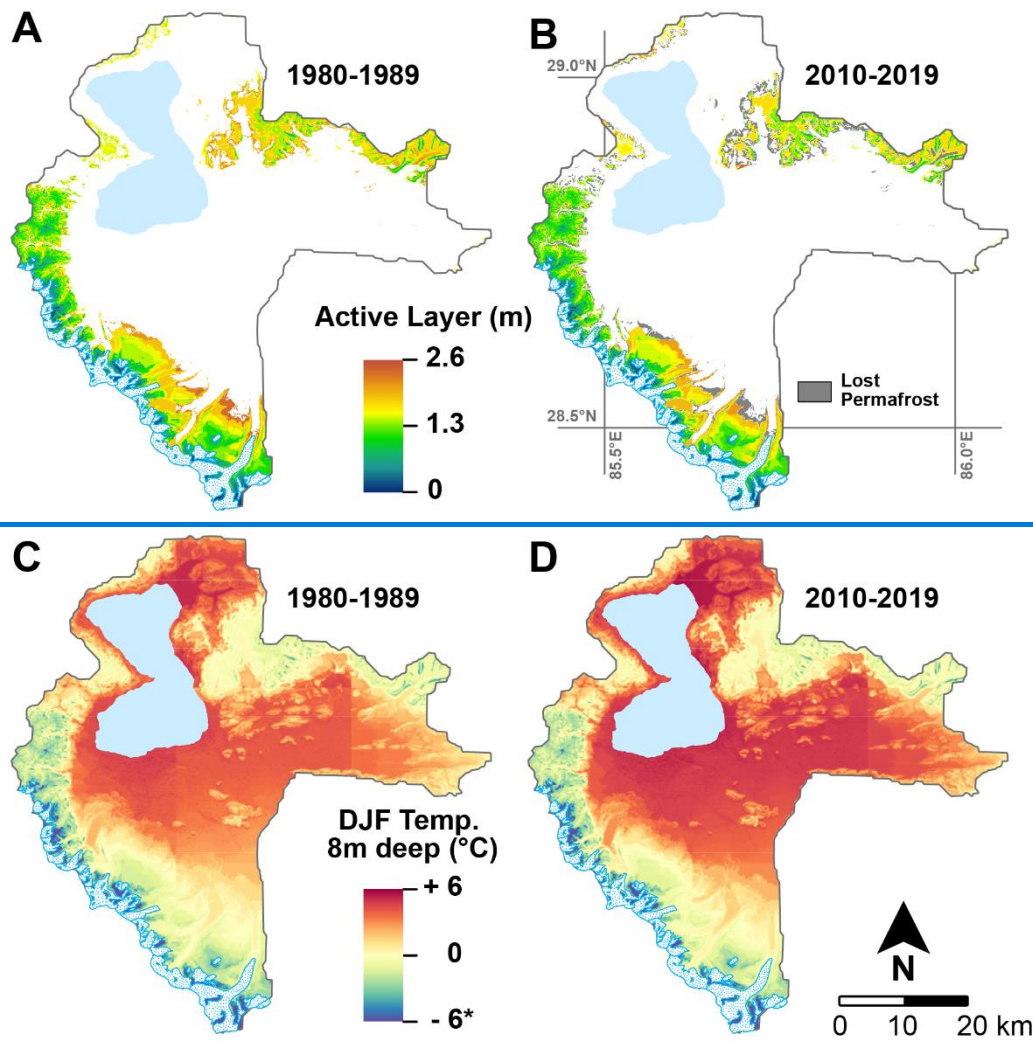
422 Over the 40 years, the average ~~yearlyannual~~ land runoff value (surface + subsurface) we model is
423 24 ± 8 mm. Summed together, the land and glacier runoff find a partial agreement with the runoff that
424 is required to close the lake water balance. ~~YearlyAnnual~~ values are compatible within error bars for 28
425 out of the 40 years of simulations. The glacier and land runoff are slightly too small to close the lake
426 water balance during the first 20 years, and slightly too large for the last 20 years of simulation. Over
427 the whole period, the sum of the glaciers + land runoff produces 95% of the required runoff. Land runoff
428 is further described in Sect. ~~4.3~~.

429 [4.3 and lake results in section 4.4.](#)

430 4.2. Ground thermal results

431 Thermal results are summarized in Fig. 6, Tab. 1 and the Fig. 7. The maps A and B of Fig. 6 show
432 the active layer thicknesses throughout the catchment, averaged for the 1980-1989 and 2010-2019
433 periods. If there is an active layer present in map A but not in map B, the permafrost disappeared during
434 the simulation (represented in grey in Fig. 6B). From 1980 to 1989, permafrost covers 27% of the
435 catchment and the mean active layer thickness is 1.36 ± 0.51 m (1σ , minimum: 0.11 m and maximum:
436 2.37 m). Based on our temperature results, we define four categories of ground thermal regimes (Fig.
437 6A). From 2010 to 2019, permafrost covers 22% of the catchment. At the scale of the initial permafrost
438 area, this change corresponds to a loss of 19%. The mean active layer thickness is 1.29 ± 0.49 m (1σ ,
439 minimum: 0.11 m and maximum: 2.55 m) for this period. Permafrost disappearance mainly happens for
440 low-lying permafrost of the south and the center of the catchment. It occurs for the most part on the
441 outer slopes of the permafrost regions and at the bottom of steep glacial valleys.

442 Maps C and D present 8-m depth temperatures fields for the months of December, January and
443 February averaged for the same two decades. While the mean temperature for the first decade of the
444 simulation is 1.83 °C, it is 2.37 °C for the last decade. This deep warming is associated with a migration
445 of the 0 °C isotherm from 5260 masl to 5320 masl (+60 m). The warming trend is not spatially uniform
446 and varies with elevation. The mean ΔT_{8m} (difference between the 2010-2019 and the 1980-1989
447 period) is the strongest at the bottom of the catchment where it reaches $+0.68 \pm 0.23$ °C for the 4500-
448 5000 masl elevation range and decreases linearly with elevation until $+0.09 \pm 0.14$ °C beyond 6000
449 masl.



450 *Figure 6. Thermal result maps. A: Average active layer depth over the 1980-1989 period. B: Average*
 451 *active layer depth over the 2010-2019 period. Only locations presenting permafrost at the end of the*
 452 *simulation are assigned a color on the map. Locations which underwent permafrost disappearance*
 453 *appear in grey on B. C: Average 8m deep ground temperature for December, January and February*
 454 *for the 1980-1989 period. D: Average 8m deep ground temperature for December, January and*
 455 *February for the 2010-2019 period.*
 456
 457

458 ~~Based on the active layer results, we define four categories of ground thermal regimes. Cold~~
 459 *permafrost* are the areas of the catchment for which the deepest thaw depth did not exceed 1 m over the
 460 40 years of simulation. For cold permafrost, frozen conditions dominate the first meters of the ground
 461 most of the year and surficial thawing during summer ~~is limited and does not give rise to a distinct~~
 462 ~~active layer season can be interrupted by ground freezing from the surface to the top of the permafrost~~
 463 ~~at night.~~ *Warm permafrost* are the areas of the catchment presenting permafrost for the whole duration
 464 of the simulation and which are not part of the *cold permafrost*. These areas are characterized by a
 465 distinct seasonal pattern of frozen ground in winter and ~~an~~ active layer in summer. *Disappearing*

466 *permafrost* are the areas of the catchment presenting permafrost at the beginning of the simulation and
 467 not at the end. *No permafrost* are the areas without permafrost at the onset of the simulation. The
 468 geographical characteristics of each ground category isare presented in Tab. 1, and their distribution
 469 throughout the catchment is shown on Fig. ~~F of the appendices 6A~~. These different ground categories
 470 are subsequently used to compare their cryo-hydrological behaviors during the simulation (consistent
 471 color code).

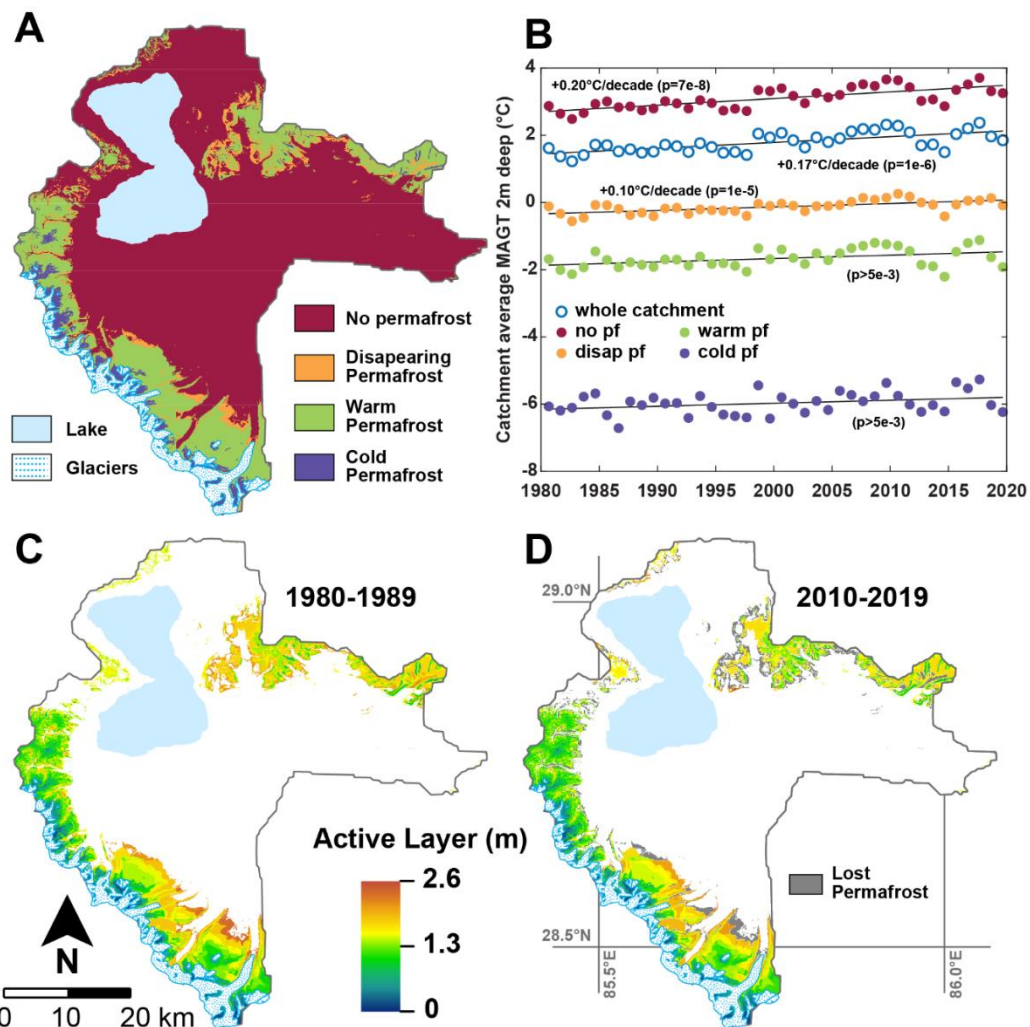
472 *Table 1. Cryological classification of the catchment based on the modeled ground temperatures.*

Name	Characteristics	% of the catchment area	Elevation mean (masl)	Elevation range (masl)	Slope mean (°)
Cold permafrost	Max thaw depth over the 40 years < 1m	3%	6068	6946 5213	35±13
Warm Permafrost	Max thaw depth > 1 m and permafrost present over the 40 years	19%	5480	5921 4877	20±9
Disappearing permafrost	Permafrost present in 1980 but disappears during the simulation	5%	5274	5552 4882	18±9
No permafrost	No permafrost from 1980 to 2019	73%	4900	5463 4580	10±8

473 ~~Fig. 7A shows the yearly temperature at a 2 m depth averaged for the whole catchment and for~~
 474 ~~each cryological state of the ground.~~ At the catchment scale, the 2 m depth temperature (Fig. 6B) shows
 475 a pronounced warming trend of 1.70.17 °C per ~~centurydecade~~ ($p=1\times 10^{-6}$). This trend is mainly
 476 supported by the *no permafrost* areas, which underwent a slightly stronger warming trend of 0.2.0 °C
 477 per ~~centurydecade~~ ($p=7\times 10^{-8}$). Areas with disappearing permafrost, warm permafrost and cold
 478 permafrost exhibit smaller trends around 0.1 °C per ~~centurydecade~~ with decreasing p-values
 479 (respectively 0.00001, 0.006 and 0.05, i.e. non-significant for the last two).

480 ~~Fig. 7B shows the average duration of seasonal thawing at a depth of 70 cm averaged over the~~
 481 ~~catchment.~~ From 1980 to 1989, permafrost covers 27% of the catchment and the mean active layer
 482 thickness is 1.36 ± 0.51 m (1σ , minimum: 0.11 m and maximum: 2.37 m, Fig. 6C). From 2010 to 2019,
 483 permafrost covers 22% of the catchment. At the scale of the initial permafrost area, this change
 484 corresponds to a loss of 19%. The mean active layer thickness is 1.29 ± 0.49 m (1σ , minimum: 0.11 m
 485 and maximum: 2.55 m, Fig. 6D) for this period. Permafrost disappearance (grey zones in Fig. 6D)

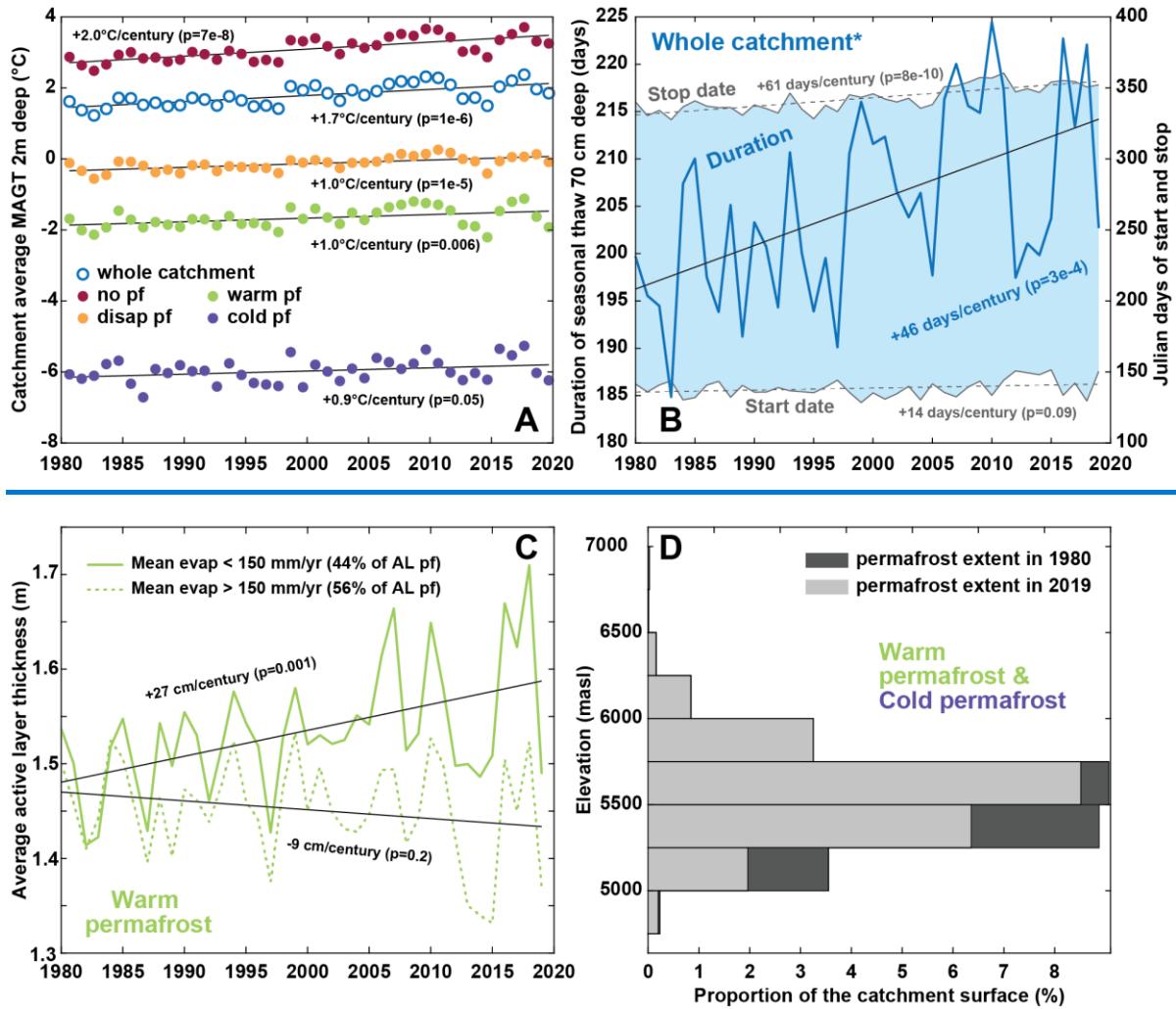
486 mainly happens for low-lying permafrost of the south and the center of the catchment. It occurs for the
 487 most part on the outer slopes of the permafrost regions and at the bottom of steep glacial valleys.



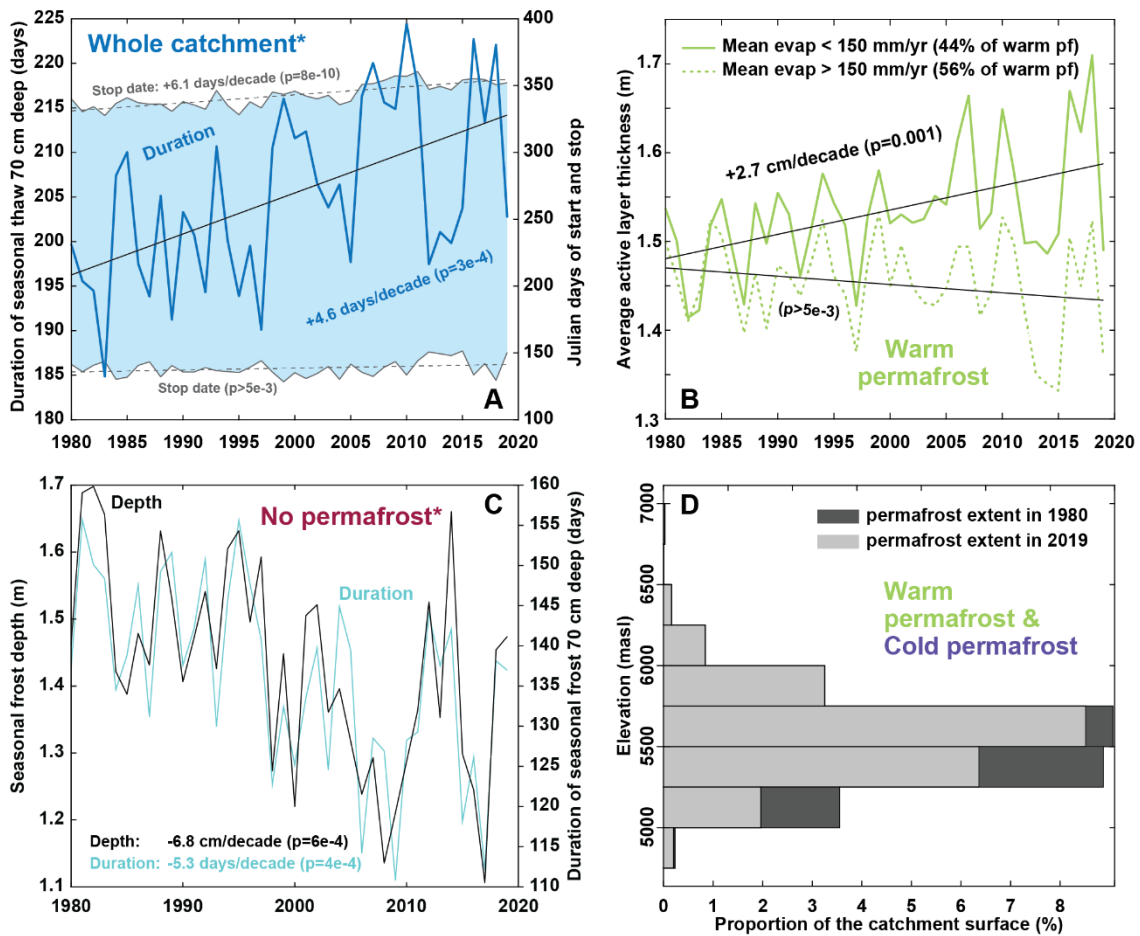
488
 489 Figure 6. A: Different cryological states of the ground throughout the catchment for the 1980-2019
 490 period (see Tab. 1). B: Annual 2 m deep ground temperature averaged for the whole catchment and for
 491 the different cryological states of the ground. C: Average active layer depth over the 1980-1989 period.
 492 D: Average active layer depth over the 2010-2019 period. Only locations presenting permafrost at the
 493 end of the simulation are assigned a color on the map on C and D. Locations where permafrost has
 494 disappeared are shown in gray on D.

495
 496 We also present the average duration of seasonal thaw at a depth of 70 cm averaged over the
 497 catchment (Fig. 7A). Because at this depth some areas might present two (or more) consecutive years
 498 without thawing (highest locations) or without freezing (lowest locations), these areas were excluded
 499 from the averaging. In the end, the averaged results account for 89% of the catchment land area (i.e.
 500 excluding glaciers and lake Paiku). The results show an increasing trend in the duration of the seasonal
 501 thaw of +464.6 days per centurydecade ($p=3 \times 10^{-4}$), blue line on Fig. 7A). When looking at the average

502 start and stop days of the seasonal thaw (Fig. 7A, grey lines) in the Julian calendar (day 150 is the 30th
 503 of May and day 300 is the 27th of October), we note that this increase is mainly caused by a later ending
 504 date of the thaw season (Stop date on Fig. 7, +61 days per century, $p=8 \times 10^{-10}$) and not
 505 by an earlier starting date (+14 days per century, $p=0.09$ (non-significant trend)).



506



507
 508 *Figure 7. Ground thermal results. A: Yearly 2 m deep ground temperature averaged for the whole*
 509 *catchment and for the different cryological states of the ground (see Tab. 1). B: duration*
 510 *of seasonal thaw 70cm 70 cm deep averaged over the catchment. The asterisk indicates that the presented*
 511 *curves average 89% of the surface of the catchment (Sect. 4.2). The grey curves and the light blue*
 512 *area are associated with the right axis and indicate the average start and stop day of the seasonal thaw*
 513 *in the Julian calendar. Values higher than 365 indicates that freezing conditions came back*
 514 *after the 31st of December. C: active layer thickness B: Active Layer Thickness (ALT) evolution for warm*
 515 *permafrost. The solid line shows the ALT for simulations experiencing a yearly annual*
 516 *evaporation lower than 150 mm when averaged over the 40 years. The dashed line shows the ALT for simulations*
 517 *with yearly evaporation higher than 150 mm. C: Temporal*
 518 *trends for seasonally frozen ground where there is no permafrost. The asterisk indicates that*
 519 *simulations were excluded if one of the simulated years did not present freezing conditions 70 cm deep*
 520 *(persistence of thawed conditions from one year to another). The presented curves thus average 88%*
 521 *of the total permafrost-free areas of the catchment. D: Altitudinal distribution of permafrost in 1980*
 522 *and 2019. This distribution includes both cold and warm permafrost.*

523
 524 *Fig. 7C shows active layer thickness trends for warm permafrost. Within warm permafrost, we*
 525 *distinguished AL thickness is presented for locations experiencing an average evaporation lower or*
 526 *higher than 150 mm per year during the simulations. (Fig. 7B). Whereas locations with average*
 527 *evaporation below 150 mm per year record an active layer deepening trend of 272.7 cm per*
 528 *century/decade (p=0.001), it is not the case for locations with an average evaporation higher than 150*
 529 *mm per year (p=0.2, non-significant trend).*

530 ~~Fig. 7D compares permafrost spatial distribution between 1980 and 2019. These~~ In the permafrost-
531 free areas of the catchment, seasonal frozen ground (Fig. 7C) reaches a depth of 1.43 ± 0.15 m on
532 average and shows a decreasing trend of -6.8 cm per decade ($p=6 \times 10^{-4}$). At a 70 cm depth, the average
533 duration of seasonally frozen ground is 136 ± 12 days with a decreasing trend of -5.3 days per decade
534 ($p=4 \times 10^{-4}$). These values average 88% of the no permafrost areas since locations showing persistent
535 thawed conditions at this depth from one year to another were excluded (i.e. minimal seasonal freezing
536 depth over the 40 years lower than 70 cm).

537 When comparing permafrost spatial distribution between 1980 and 2019 (Fig. 7D), our results
538 show that permafrost distribution above 5750 masl has not been modified during the simulation.
539 Permafrost disappearance has mainly occurred between 5000 and 5750 masl, with the largest loss
540 reaching 2.5% of the catchment area between 5250 and 5500 masl.

541 ~~In the permafrost free areas of the catchment, seasonal frozen ground reaches a depth of 1.43 ± 0.15~~
542 ~~m on average and shows a decreasing trend of -6.8 cm per century ($p=6 \times 10^{-4}$, Fig. E). At a 70 cm depth,~~
543 ~~the average duration of seasonal frozen ground is 136 ± 12 days with a decreasing trend of -5.3 days per~~
544 ~~century ($p=4 \times 10^{-4}$). These values average 88% of the no permafrost areas since locations showing~~
545 ~~persistent thawed conditions from one year to another were excluded.~~

546 4.3. Hydrological results for the land

547 ~~Hydrological results are summarized on Fig. 8. Fig. 8A shows the yearly~~ The mean annual
548 evaporation averaged over the whole catchment (land area only). The mean yearly evaporation over
549 the simulation time is 180 ± 19 mm (1σ , Fig. 8A). Evaporation shows an increasing trend over the 40
550 years of ~~+101~~ 1.01 mm per ~~century~~ decade ($p=3 \times 10^{-7}$). Average total runoff over the 40 years is 24 ± 8
551 mm per year (Fig. 8B) and exhibits an increasing trend of ~~+484.8~~ 484.8 mm per ~~century~~ decade ($p=8 \times 10^{-7}$).
552 Similarly, surface runoff (13 ± 3 mm per year) and subsurface runoff (11 ± 6 mm per year) show
553 increasing trends of ~~+131.3~~ 131.3 and ~~+353.5~~ 353.5 mm per ~~century~~ decade ($p=6 \times 10^{-5}$ and 3×10^{-7}) respectively. (Fig.
554 8B). The surface runoff presented on Fig. 8B includes the snow melt that did not infiltrate the ground.

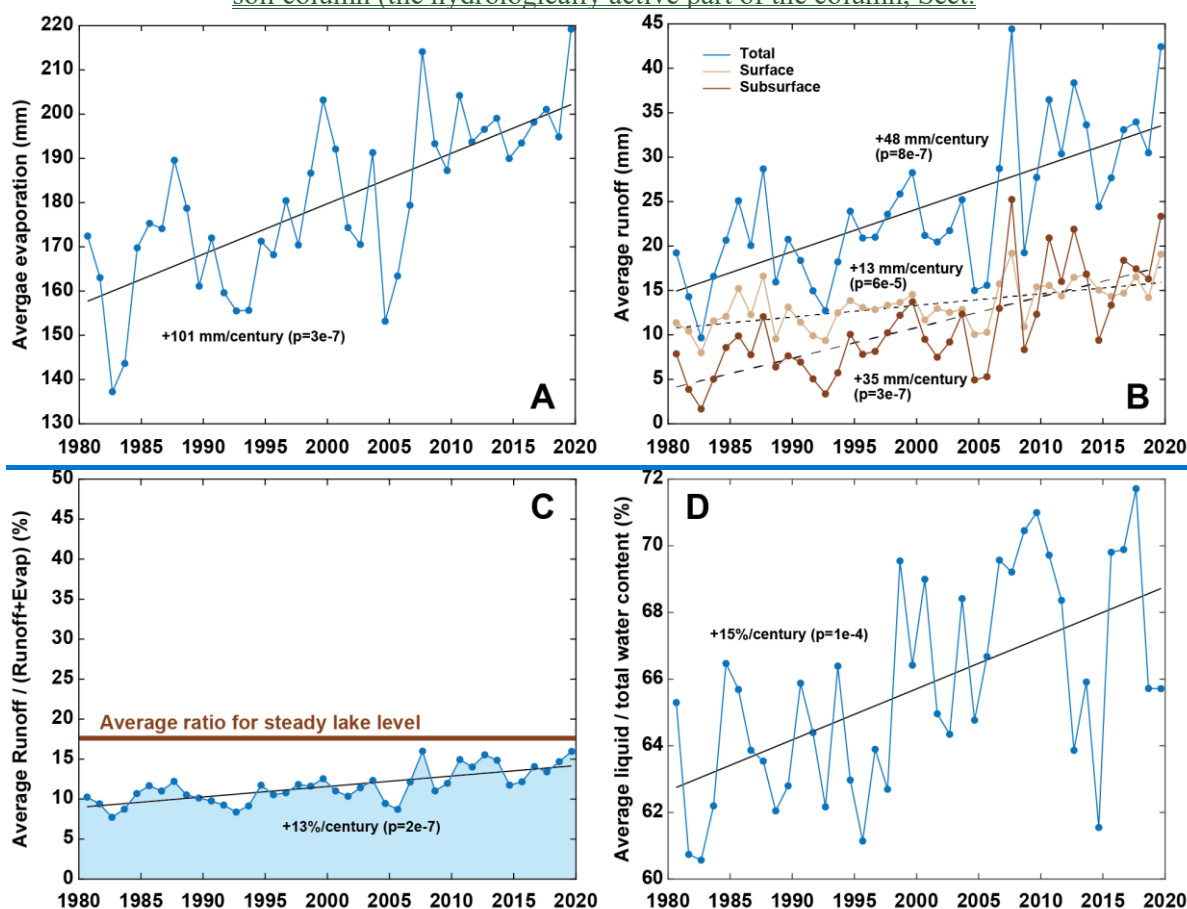
555 These linear trends we report are high compared to the absolute values of the variables and their
556 extrapolation backward in time would lead to null values in the recent past which is unrealistic. This
557 suggests a non-linear evolution of these variables over the XXth century.

558 Fig. 8C presents We also present the catchment average of the *runoff* / (*runoff* + *evaporation*) ratio;
559 (Fig. 8C), which is equivalent to *runoff* / (*rain* + *snow* - *snow sublimation*) given the
560 ~~negligeable~~negligible contribution of soil storage variations. Hence it is the proportion of the water
561 input to the ground surface that is converted into runoff. This proportion is $11 \pm 2\%$ over the simulation
562 time and shows an increasing trend of ~~+13~~1.23% per ~~century~~decade ($p=2 \times 10^{-7}$). ~~Fig. The graph~~8C also
563 shows the average theoretical ratio to maintain a steady lake level (of 17.6%-%). This ratio was obtained
564 under the following hypothesis:

- 565 • Same climate forcing data, hence same lake evaporation
- 566 • The glacier contribution is (i) considered the same for the historical simulation and this
- 567 scenario and (ii) taken as the difference between the total land surface runoff and the red
- 568 curve of *required runoff* [eain](#) figure 5, therefore independent of remotely sensed estimates.
- 569 • Under these conditions, the runoff increase needed to maintain the lake level is only
- 570 supplied by land runoff (surface and subsurface) by shifting the *runoff / (runoff +*
- 571 *evaporation)* ratio.

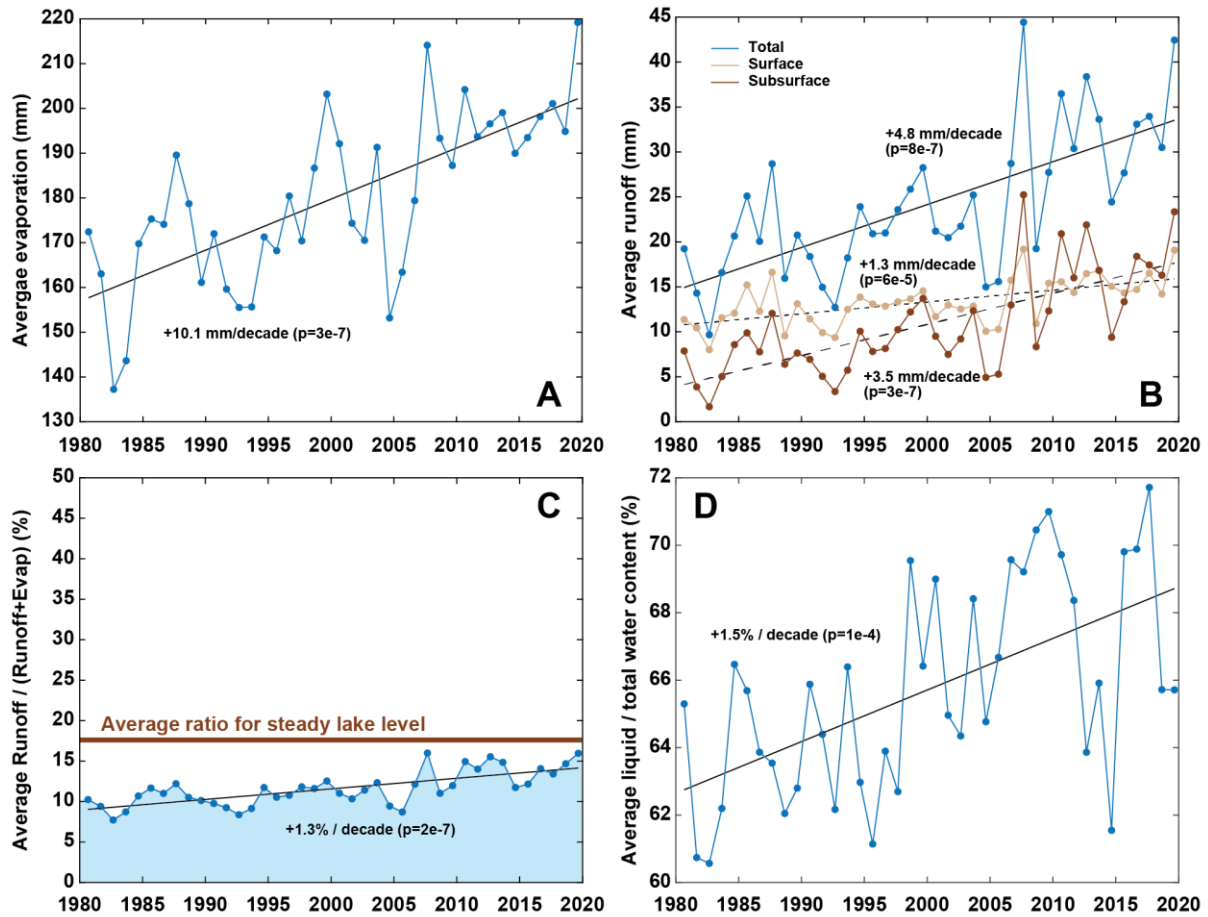
572 The ~~graph shows that the~~ ratio from the historical simulation starts significantly below the
 573 theoretical steady lake ratio (10.2% < 17.6%)%, [Fig. 8C](#)) and increases progressively to 16.0% in 2019.
 574 ~~This evolution is consistent with observations that show a progressive stabilization of the lake level~~
 575 ~~(Fig. 5).~~

576 [Finally, Fig. 8D shows the annual proportion of liquid / total water averaged for the whole catchment.](#)
 577 [The value was computed based on the daily water content \(liquid and frozen\) of the first 2 m of the](#)
 578 [soil column \(the hydrologically active part of the column, Sect.](#)



579

580 3.2.4) from which annual averages were derived and used to compute a catchment scale average.
581 The graph indicates that the proportion of liquid water in the total water content increases at around
582 +1.41% per decade ($p=1\times 10^{-4}$), indicating an increasing availability of liquid water in the ground with
583 time.



584
585
586
587
588
589
590
591
592
593

Figure 8. Hydrological results. A: yearly Annual evaporation averaged over the whole catchment. B: yearly Annual runoff averaged over the whole catchment. The blue curve sums the surface and subsurface runoff. C: Ratio between runoff and (evaporation + runoff) averaged over the whole catchment. The brown line indicates the theoretical average ratio needed to maintain a steady lake level when considering an identical glacier contribution to runoff (details in Sect. 4.3). D: Yearly Annual mean of the (liquid water)/(liquid water + frozen total water) ratio over the first 2 meters of ground, averaged over the whole catchment.

4.4. Hydrological budget of Lake Paiku

Our observations, climate data, simulations, geodetic data and the lake level data from Lei et al. (2018, 2021) enables us to quantify the different terms of the lake hydrological budget. We present these results in m of lake level change based on the average slope of the Volume = $f(\text{level})$ relationship (Fig. 9). As the unique output term, evaporation dominates the lake budget with an average annual value of 0.86 m (34.6 m / 40 years, Fig. 9A). Direct precipitation in the lake is the dominant input with an average annual value of 0.31 m (12.3 m / 40 years), followed by glacier runoff (0.28 m/yr, 11.3 m / 40 years) and land runoff (0.18 m/yr, 7.0 m /40 years). When compared with lake volume observations over the 40 years of the simulation period, the simulated lake budget is 1.04 m too negative.

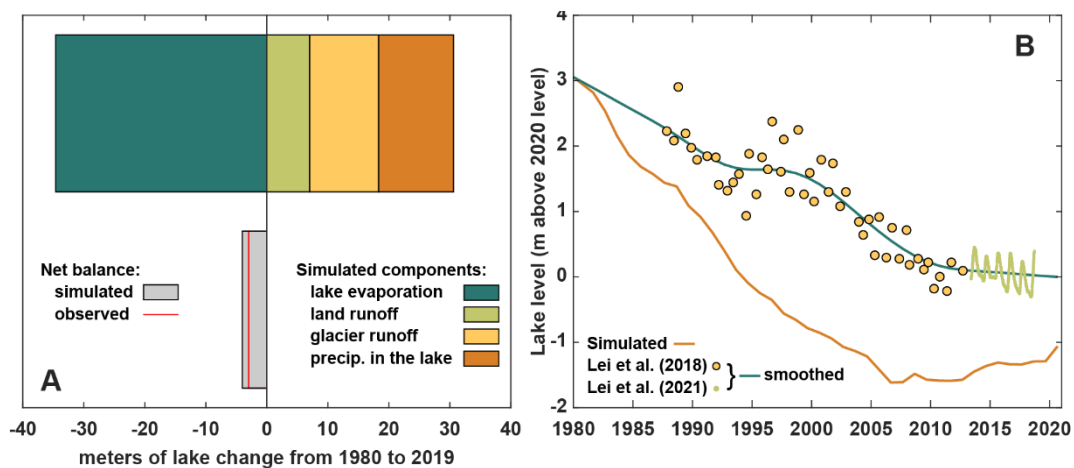


Figure 9. Budget and level of lake Paiku for the simulation period (1980-2019). A. The different components of the hydrological budget of the lake according to our framework. Results are given in m of lake change based on the average slope of the Volume = $f(\text{level})$ relationship. B. Lake level data. Points correspond to observations from Lei et al. (2018, 2021) that we smoothed (green curve, based also on observation points older than 1980). The simulated lake level appears in orange.

Based on our results, we also reconstructed lake level variations that we compare with the observed variations (Fig. 9B). Following our framework, our values are presented at an annual timestep. They qualitatively reproduce the overall lake level decrease but tend to overestimate this decrease and show an increasing mismatch with the observations from 0 in 1980 to 2 meters in 2005. This mismatch is later compensated by an increasing lake level trend in our simulation from 2005 to 2019. At the end of the simulation period, the mismatch is 1.04 m, consistent with the budget values (Fig. 9A) and the fact that our approach provides 95% of the required runoff to close the lake budget (Sect. 4.1.). This pattern

616 of a too strong decrease followed by an increase is consistent with the comparison between simulated
617 and required runoff presented on Fig. 5D.

618 ~~Finally, Fig. 8D shows the yearly proportion of liquid / (liquid + frozen) water averaged for the~~
619 ~~whole catchment. The value was computed based on the daily water content (liquid and frozen) of the~~
620 ~~first 2 m of the soil column (the hydrologically active part of the column, Sect. 3.2.4) from which yearly~~
621 ~~averages were derived and used to compute a catchment scale average. The graph indicates that the~~
622 ~~proportion of liquid water in the total water content increases at around +15% per century ($p=1\times 10^{-4}$),~~
623 ~~indicating an increasing availability of liquid water in the ground with time.~~

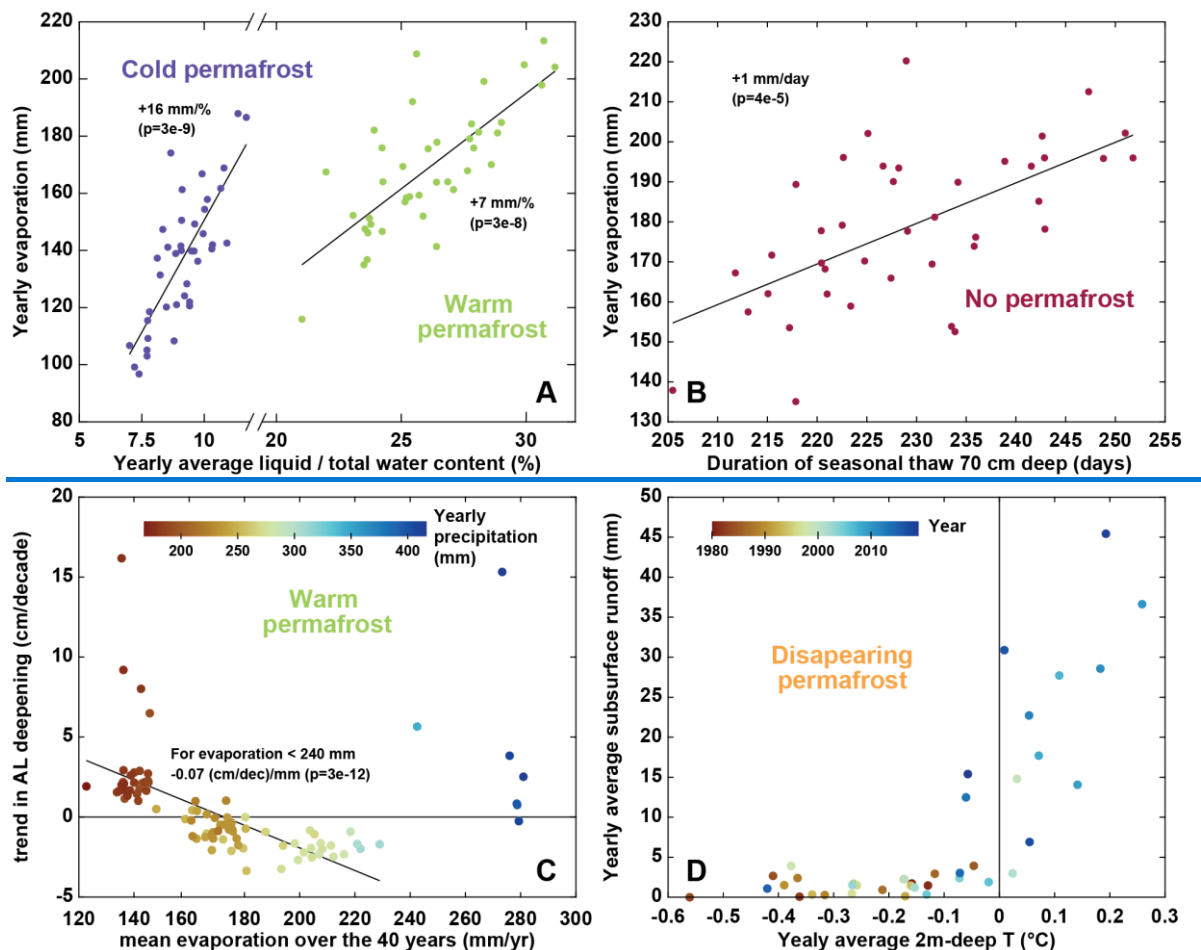
624 4.4. Thermo-hydrological couplings

625 ~~Fig. 9 presents simulation results highlighting the interplay between the fluxes of energy and water~~
626 ~~at the surface and the subsurface and relating the ground temperature to the water content. Fig. 9A~~
627 ~~shows the correlation between the yearly liquid / (liquid + frozen) water ratio in the first 2 m of the~~
628 ~~ground and the yearly evaporation for cold permafrost and warm permafrost. The graph highlights that~~
629 ~~higher evaporation is observed during the years with higher availability of liquid water in the ground.~~
630 ~~Fig. 9B shows the correlation between the duration of the seasonal thaw and the yearly evaporation for~~
631 ~~no permafrost areas of the catchment. It shows that years with longer seasonal thaw tend to be associated~~
632 ~~with higher yearly evaporation.~~

633 ~~Fig. 9C tests the relationship between the linear trend of active layer deepening and the mean~~
634 ~~evaporation (over the 40 years of simulation) for warm permafrost areas. Thus, this graph does not~~
635 ~~present yearly values and one point corresponds to one of the 92 simulations classified as warm~~
636 ~~permafrost (values based on the 40 years). The graph highlights that simulations showing an AL~~
637 ~~deepening trend are associated with low evaporation. From there, simulations with stronger evaporation~~
638 ~~show no deepening trend or even a shrinkage of the AL. This relationship is contradicted for the highest~~
639 ~~level of evaporation observed for warm permafrost, for which AL deepening is observed again (dark~~
640 ~~blue points of the graph). These simulations with the highest levels of evaporation also correspond to~~
641 ~~those receiving the largest amount of precipitation.~~

642 ~~Finally, Fig. 9D displays the yearly values of subsurface runoff against the yearly average 2 m~~
643 ~~deep temperature for disappearing permafrost. The color scale of the points indicates the time of the~~

644 simulation. Consistent with the substantial warming trend observed for disappearing permafrost (Fig.
 645 7A) and the increase of subsurface runoff at the catchment scale (Fig. 8B), subsurface runoff shows
 646 higher values during the year that record a positive 2 m deep mean annual temperature. The average
 647 annual runoff when the 2 m deep temperature is positive is 23 ± 13 mm whereas it is 2 ± 3 mm for
 648 negative 2 m deep temperature (mean annual value).



649 *Figure 9. Thermo-hydrological couplings. A: yearly evaporation vs. yearly mean of the*
 650 *liquid / (liquid + frozen) water ratio over the first 2 meters of ground, averaged for simulations*
 651 *corresponding to cold permafrost and warm permafrost (one dot per year for each permafrost*
 652 *category). B: yearly evaporation vs. duration of seasonal thaw at a 70 cm depth averaged for*
 653 *simulations corresponding to locations without permafrost (one dot per year). C: Active layer*
 654 *deepening trend vs. mean evaporation over the 40 years for each simulation corresponding to warm*
 655 *permafrost (here one dot corresponds to one 40 years long simulation). The color of the dots shows the*
 656 *precipitations averaged over the 40 years for each simulation. The linear regression excludes*
 657 *simulations exhibiting yearly evaporation higher than 240 mm. D: Yearly subsurface runoff vs. Yearly*
 658 *2 m deep temperature averaged for simulations corresponding to locations with disappearing*
 659 *permafrost (one dot per year). The color of the dot indicates the year of the simulation.*
 660

5. Discussion

5.1. Limitation and potential of the approach

5.1.1. *Data usage within the conceptual framework and data scarcity*

The approach we develop in the present study to quantify the thermo-hydrological regime of the Paiku catchment presents both advantages and limitations that can frame discussions on the presented results. Regarding the limitations, we identify two main points. The first limitation is related to the limited amount of available field observations required to provide robust model parameterizing, climate forcing and in-depth validation of the simulations. Regarding the ground stratigraphy and parameters, in the absence of direct observations, we made use of large-scale data sets (Schaaf and Wang, 2015; Shangguan et al., 2013, 2017; Simons et al., 2020). Even though these datasets are intended to inform numerical modeling, field observation would bring additional confidence in the values we use. Regarding climatic forcing data, our AWS measurement offers sound observations to evaluate and adjust the ERA5 data processed with TopoSUB and downscaled with TopoSCALE. Yet a period of observations longer than 2 years would have brought more robust corrections and could have allowed to perform quantile mapping. Regarding the simulated temperature fields, the comparison with the loggers bring confidence that the model captures both the surface temperature mean values and seasonal patterns, but the validation exercise would benefit from additional loggers located throughout the catchment and ideally also temperature profiles from boreholes. Similarly, even though the lake evaporation values we compute finds a good agreement with those from Lei et al. (2021), a longer comparison would have brought a higher level of confidence in the values.

Finally Our approach relies on a variety of data regarding their scientific focus (glaciers, ground, lake, atmosphere), their type (in situ observations, remotely sensed data, reanalysis data), their characteristics (point wise data, distributed data, constant or with various time resolution) and the way they interact with our models (model parameters, forcing data, validation data, result data in case of the glacier runoff). Such a diversity arises from our goal to quantify both the ground thermo-hydrological regime and the different terms of the lake budget. This variety also makes it challenging to consistently merge these data into a unique framework. For example, our quantification of the glacier mass change

688 reconstruction is made of two constant values for the study period (1975-2000 and 2000-2020), which
689 limits the relevance of the comparison between the observed lake level variations and the simulated
690 ones.

691 Yet, the lake level variations are the only hydrological observations available to evaluate the
692 robustness of the runoff we compute. WeTherefore, we had to combine lake level observations with our
693 precipitation forcing data and lake evaporation quantifications in a simple mass conservation
694 calculation, to derive the land runoff to the lake required to reproduce the level variations (red curve on
695 Fig. 5). The5D). In this regard, the sum of the glacier and land runoff we derive over the 40 years
696 correspond to 95% of the required runoff to the lake, indicating that the magnitude of our reconstruction
697 is correct. Year-to-year comparison is less accurate and we suggest that this is the consequence of the
698 aforementioned limitations regarding data scarcity (including the simplifications of glacier runoff to 2
699 constant values over the 1980-2000 and 2000-2019 periods) and also of our modeling strategy as
700 detailed below.

701 A main limitation regarding our usage of the data is related to the limited amount of available field
702 observations required to provide robust model parameterizing, climate forcing and in-depth validation
703 of the simulations, both hydrologically and thermally. Regarding climatic forcing data, our AWS
704 measurement offers sound observations to evaluate and adjust the ERA5 data processed with TopoSUB
705 and downscaled with TopoSCALE. Yet, a period of observations longer than 2 years would have
706 enabled more robust corrections and could have allowed us to perform a more advanced statistical
707 downscaling approach, e.g. quantile mapping (Thiemeßl et al., 2011). As such, the spatiotemporal
708 domain of relevance of these corrections is insufficient to correct data for the whole catchment and the
709 40 years of simulations. Overall, considering the strong bias we observe in the raw ERA5 data (Figure
710 D0), these corrections do represent an important first-order improvement.

711 *5.1.2. Modeling strategy*

712 An important limitation in the modeling strategy we implement is the absence of water routing
713 throughout the catchment. First, water routing could highlight physical processes that our
714 implementation cannot represent such as the evaporation of water during its transport towards the lake,

715 ~~or downstream soil water content increase due to upstream runoff. In this regard, the best our approach~~
716 ~~can provide is to average these processes over time by closing the catchment water budget on the long~~
717 ~~run. We suggest that our simulations reach this goal, considering it produces 95% of the required runoff~~
718 ~~over the 40 years we study.~~

719 ~~Second, by~~ By giving access to the timing of water transport across the catchment, water routing
720 would allow to investigate temporal hydrological patterns at a monthly or seasonal scale. Because we
721 work at ~~yearly~~ annual and decadal time scales, this limitation has limited consequences on our results.
722 The main consequence is to ignore potential storage effects on the land that would delay the arrival of
723 runoff to the lake. We suggest that this limitation contributes to explaining the limited match between
724 computed and required runoff at ~~a yearly~~ the annual time scale. Yet, our subdivision of the catchment
725 based on the different cryological states of the ground allows us to work with hydrological units that
726 are smaller than the catchment and thus present shorter hydrological response time to precipitation.

727 Conversely, our approach also conveys several important advantages regarding our goal to
728 describe and quantify the ground thermo-hydrological regime of the catchment. The use of TopoSUB
729 enables us to produce results at a resolution of 100 x 100 m over an area of nearly 2400 km² with
730 calculation costs 700 times lower than if each 100 x 100 m pixel was treated individually. Yet, thanks
731 to the clustering method used to produce the forcing dataset (Sect. 3.2.2), the strong spatial variability
732 of the physiography and its impact on the climate and incoming radiations is significant in the forcing
733 data and has a major influence on the ground thermo-hydrological results, as exemplified by the strong
734 spatial variability of ground temperatures (Fig. 6). Beyond elevation, other physiographic parameters
735 such as aspect also influence the results. The mean values of 2 m-deep temperature and evaporation
736 over the 40 years for north-facing areas (averaged over the whole catchment and over the 40 years) are
737 ~~of~~ 1.3 °C and 163 mm while they reach 2.9 °C and 197 mm for the south-facing ones. This strong
738 ~~dependance~~ dependence of modeled results on physiography ~~highlight~~ highlights the necessity to take it
739 into account when modeling the thermo-hydrological regime of the ground in high mountainous
740 environments. Finally, our approach allows us to couple the physical processes governing both energy
741 and water fluxes at the surface and subsurface and highlight their interplay, as developed in ~~the~~
742 following section 5.1.4.

5.1.3. Reconstruction of the Lake hydrological budget and level variations

The total lake level change we simulate is a decrease of 4.11 m. This is qualitatively consistent with the overall observed trend. The mismatch with the observations is limited to a 1.06 m excess in the simulated level drop (Fig. 9A). Our reconstruction shows a decrease of 4.66 m from 1980 to 2007, which is an overestimation of the initial drop. Afterwards, while observations indicate a gradual slowdown of the lake level decrease, we simulate a stabilization followed by a slight increase (0.55 up between 2013 and 2019).

A possible reason for this mismatch is that the lake is connected to a larger aquifer that surrounds it. In the context of a decreasing lake level, an aquifer surrounding the lake can create an additional water inflow when the lake level passes below the piezometric level of the aquifer. Such an inflow could mitigate the lake level decrease and thus explain the missing water in our reconstruction. It could also explain the gradual stabilization of the lake level that our model does not reproduce. This flow is not part of our conceptual hydrological framework even though it likely exists in reality, especially since there is no permafrost near the lake (as we simulate it here), allowing for the existence of such an aquifer (Walvoord and Kurylyk, 2016). Ground water has been identified as a potential contributor to lake level rise in other regions of the QTP (Lei et al., 2022). Yet, this potential effect is difficult to account for and its magnitude remains unclear. Therefore, the reasons for the mismatch between observed and simulated lake levels could also be connected to other aspects of our methodology such as bias in the climatic forcing data and other shortcomings arising from the lack of field data, or hydrological processes, as developed in Sect. 5.1.1 and 5.1.2.

Our reconstruction of the lake budget is informative regarding the respective contribution of the different inputs and outputs. Regarding lake evaporation, our mean value of 870 ± 23 mm is close to the one modelled by Yang et al. (2016) with the Flake model for lake Nam (832 ± 69 mm) for the period 1980-2014 but we do not report a significant increasing trend in our results. Yet for the same lake (Nam Co) and a similar period (1980-2016) Zhong et al. (2020) reported an average value of 1149 ± 71 mm (along with an increasing temporal trend) using the Penman formula (Penman, 1948), thus highlighting the potential dependence of the results to the methodology. In our results, direct precipitation to the lake

770 represents 40% of the inputs, followed by glacial runoff (35%) and land runoff (25%). Glaciers are
771 therefore a particularly important contributor to the runoff towards the lake (60% of the total runoff, vs.
772 40% for land runoff), what contrasts with the results from Biskop et al. (2016) who calculated that the
773 runoff input to the lake Paiku was dominated by land runoff (70% and 30% for the glacier contribution).
774 Here again, these difference likely arises from important differences in input data and methodologies
775 to quantify the different hydrological processes (evaporation, runoff, snow and glacier melt). Yao et al.,
776 (2018) reported that, at the OTP scale, the balance between precipitation and evaporation (over land
777 and lake) was dominant over glacier melt to understand both lake storage increases and decreases. Our
778 reconstruction does not give us access to significant temporal variation of the glacier contribution but
779 the above-mentioned proportions in the contributions to the lake (40%, 35% and 25%) show that the
780 glacier contribution does not dominate the input terms. At the catchment scale, these proportions can
781 vary significantly depending on the glacier coverage. For Lake Selin, Zhou et al. (2015) reported that
782 runoff towards the lake, evaporation from the lake and on-lake precipitation altogether explained 90%
783 of the lake storage variations for the 2003-2012 period. The catchment of lake Selin exhibits a very
784 limited glacier coverage (0,63% of its area, Lei et al., 2013) compared to the Paiku (5%).

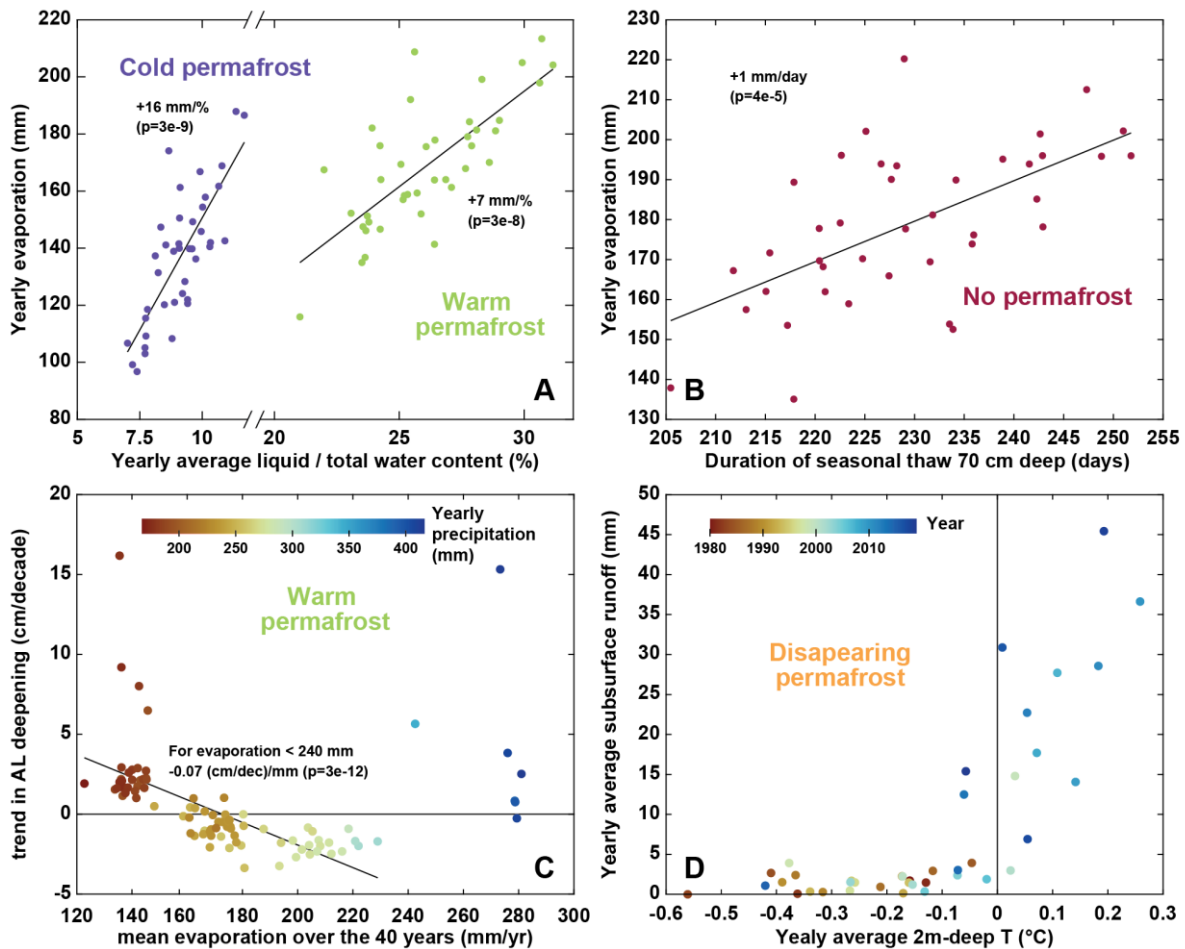
785 5.1.3.5.1.4. The interdependence of thermal and hydrological variables

786 Results presented in Sect. 4.4 highlight how water and Our simulation results enable us to explore
787 the interplay between the fluxes of energy fluxes and water at the surface and subsurface are coupled.
788 In this regard, we tested the correlation of evaporation with the proportion of liquid/total water in the
789 ground for cold and warm permafrost, as well as the correlation between evaporation and the duration
790 of seasonal thaw at a 70 cm depth (Fig. 10A and B). For permafrost areas (cold permafrost and warm
791 permafrost), evaporation shows a strong ~~connection~~ correlation with the seasonal distribution between
792 liquid and frozen water, similarly similar to previous modeling works for the region (Cuo et al., 2015).
793 As such, this correlation suggests that the intensity of seasonal ground thaw plays a major role in
794 enabling higher or lower evaporative fluxes because. This is likely due to cold surface temperatures
795 strongly reducing water loss from the surface and because moisture delivery to the surface is
796 inhibited when the ground is frozen. We suggest that this dependance dependence is particularly

797 important in the Paiku Catchment because evaporation is strong (88% of the precipitation input to the
798 surface evaporates on average) and because frozen water is the dominant form of water in the ground
799 in permafrost areas (Fig. 9B10A, the calculation includes the first 2 meters below the surface).

800 Similarly, evaporation in *no permafrost* areas shows a ~~connections~~significant correlation with the
801 duration of the seasonal thaw. ~~Because (Fig. 10B). We suggest that this result arises from the fact that~~
802 frozen ground limits the evaporative fluxes, ~~and thus~~ years during which the subsurface seasonal thaw
803 is shorter are associated with reduced evaporative fluxes. ~~We also tested the relationship between the~~
804 linear trend of active layer deepening and the mean evaporation (over the 40 years of simulation) for
805 warm permafrost areas (Fig. 9B). 10C). Thus, this graph does not present annual values and one point
806 corresponds to one of the 92 TopoSUB points classified as warm permafrost (values based on the 40
807 years). The graph highlights that TopoSUB points showing an AL deepening trend are associated with
808 low evaporation and precipitation. From there, TopoSUB points with stronger evaporation show no
809 deepening trend or even a shrinkage of the AL. This relationship is contradicted by the highest level of
810 evaporation observed for warm permafrost, for which AL deepening is observed again (dark blue points
811 of the graph). These TopoSUB points with the highest levels of evaporation also correspond to those
812 receiving the largest amount of precipitation. Further discussion on active layer trends is provided in
813 the next section.

814 Runoff also shows a strong connection with the ground thermal regime ~~and~~ (Fig. 9D ~~highlights~~
815 ~~how changes in the ground thermal regime correspond to modifications in the hydrological pathways~~
816 ~~for disappearing permafrost. 10D). At the beginning of the simulation, years with an average 2 m-deep~~
817 ~~frozen condition~~ temperature below 0 °C are associated with limited subsurface runoff (< 5 mm per
818 year). Over the years, as the ground warms up and permafrost disappears, subsurface runoff increases
819 and can reach 20 to 45 mm per year. This result is consistent with increased subsurface connectivity
820 expected when permafrost thaws (Gao et al., 2021; Kurylyk et al., 2014) that has been both observed
821 ~~(Chiasson-Poirier et al., 2020; Niu et al., 2016)~~ (Niu et al., 2016) and modeled (Gao et al., 2018; Huang
822 et al., 2020; Lamontagne-Hallé et al., 2018). We suggest that these substantial changes in subsurface
823 runoff, associated with changes in the ground temperature in Fig. 10D support the hypothesis of a
824 modification in the hydrological pathways as permafrost thaws.



825
 826 *Figure 10. Thermo-hydrological couplings. A: Annual evaporation vs. annual mean of the liquid / total*
 827 *water ratio over the first 2 meters of ground, averaged for simulations corresponding to cold permafrost*
 828 *and warm permafrost (one dot per year for each permafrost category). B: Annual evaporation vs.*
 829 *duration of seasonal thaw at a 70 cm depth averaged for simulations corresponding to locations without*
 830 *permafrost (one dot per year). C: Active layer deepening trend vs. mean evaporation over the 40-year*
 831 *for each simulation corresponding to warm permafrost (here one dot corresponds to one TopoSUB*
 832 *point). The color of the dots shows the precipitations averaged over the 40 years for each simulation.*
 833 *The linear regression excludes simulations exhibiting annual evaporation higher than 240 mm. D:*
 834 *Annual subsurface runoff vs Annual 2 m-deep temperature averaged for simulations corresponding to*
 835 *locations with disappearing permafrost (one dot per year). The color of the dot indicates the year of*
 836 *the simulation.*

837
 838 Altogether, these results ~~highlight the dependance~~suggest a dependence of key variables
 839 quantifying the catchment hydrological balance (evaporation, runoff) to the seasonal characteristics and
 840 interannual trends of the ground thermal regime (temperature, liquid vs frozen water content).
 841 ~~Similarly~~Similar to previous studies (Ding et al., 2020; Wang and Gao, 2022), ~~these results advocate~~
 842 ~~for the necessity to couple thermal and hydrological modeling to improve our ability to understand and~~
 843 ~~quantify changes in the hydrological balance of high mountain catchments. To our best knowledge, we~~
 844 ~~think these results advocate for the necessity to couple thermal and hydrological modeling to improve~~

845 [our ability to understand and quantify changes in the hydrological balance of high mountain catchments.](#)
846 [To our best knowledge, along with Gao et al. \(2022\),](#) our study represents to date the most complete
847 effort to include the variety of coupled climatological, surface and subsurface processes characterizing
848 the climate, hydrology and ground thermal regime of high-mountain catchments in Tibet at a small
849 scale with a high spatial resolution.

850 5.2. Cryo-hydrological trends in the catchment and across the QTP

851 5.2.1. Permafrost and ground temperature changes

852 Our results indicate that permafrost coverage in the Paiku catchment ~~evolves~~[evolved](#) from 27 to
853 22% of the land area during the simulated period. Such a coverage corresponds to sporadic permafrost
854 (10-50% of the area) and is consistent with recent large-scale estimates of permafrost in the
855 ~~northern~~[Northern](#) Hemisphere (Obu et al., 2019) and across the QTP (Ran et al., 2018; Zou et al., 2017).
856 This decrease corresponds to a 19% shrinkage of the 1980 permafrost area, which is ~~more~~
857 ~~important~~[higher](#) than the 9% reported by Gao et al. (2018), [a value](#) determined by catchment-scale
858 numerical modeling in the upper Heihe catchment (northeastern QTP) over a similar period. It is also
859 slightly higher than the 13% decrease modeled from 1971 to 2015 for the Qinghai Lake catchment with
860 a similar approach by Wang and Gao (2022). Yet, it is smaller than the 34% loss modeled by Qin et al.
861 (2017) from 1981 to 2015 for the Yellow River Source Region (YRSR, North Eastern QTP).

862 Active layer (AL) evolution is ~~contrasted~~[contrasting](#) throughout the catchment and a deepening
863 signal is only visible for the locations with limited evaporation (<150 mm per year). Given the strong
864 drive of summer climate on Active Layer Thickness (ALT), this overall lack of a deepening trend
865 highlights how evaporation can act as an energy intake at the surface, ~~limiting the subsurface heat fluxes~~
866 ~~and thus AL deepening~~ (Yang et al., 2014a), [limiting the surface and subsurface heat fluxes and thus](#)
867 [AL deepening](#). In this regard, our results fall in line with the conclusions of Fisher et al. (2016) when
868 observing evapotranspiration and ALTs in boreal forests and also confirm the modeling experiments of
869 Zhang et al. (2021b) on permafrost wetting in arid regions of the QTP. Besides, the lack of [an](#) overall
870 deepening trend is consistent with observations from Luo et al. (2018) in the YRSR over the last decade
871 and with the modeled AL from Zhang et al. (2019) at the scale of the QTP for the last 40 years. Where

872 evaporation is limited, we report an AL deepening trend of 2.7 cm per decade ~~that, which~~ is smaller
873 than the 4.8 cm per decade trend modeled by Song et al. (2020) for the YRSR for the same period, and
874 smaller than the 4.3 cm modeled by Gao et al (2018) in the upper Heihe catchment. Yet it is
875 ~~similar~~comparable to the 2 cm per decade value modeled by Wang and Gao (2022) for the Qinghai
876 Lake catchment from 1971 to 2015.

877 In *no permafrost* areas, our simulations show that the thickness of ~~seasonal~~seasonally frozen
878 ground shrinks at a rate of 6.8 cm per decade. This rate is faster than the rate of 3.1 cm per decade
879 quantified by Qin et al. (2018) using the Stefan solution for the YRSR (1961-2016) and faster than the
880 3.2 cm per decade modeled by Gao et al. (2018, Heihe catchment). However, it is similar to the 6 cm
881 per decade rate modeled by Wang and Gao (2022) in the Qinghai Lake catchment from 1971 to 2015
882 and smaller than the 12 cm per decade modeled by Qin et al. (2017) for the YRSR (1981-2015). All
883 these values fall within the wide range of 3 to 29 cm per decade reported by Wang et al. (2020a) when
884 studying ~~seasonal~~seasonally frozen ground over the whole QTP with in-situ observations.
885 ~~Regrading~~Regarding timing, we report a decreasing trend of 5.3 days of frozen conditions (70 cm deep)
886 per decade which is consistent with the decrease of 6.7 days per decade reported by Wang et al. (2020a)
887 just below the surface.

888 Regarding the timing of seasonal ground thaw, our results highlight that the increase in the duration
889 in the seasonal ground thaw (at 70 cm) is mostly driven by a progressive delay of the end date of the
890 thaw period. This result contrasts with those from Song et al. (2020) for the same period in the YRSR
891 who also modeled an increase ~~in~~of the seasonal thaw (at a 2 cm depth) ~~but,~~ although driven by an
892 advancing trend of the start date of the seasonal thaw.

893 Our warming trends at a 4 m depth for permafrost areas is 0.1 °C per decade, which is substantially
894 smaller than the 0.43 °C per decade observed at this depth between 1996 and 2006 in permafrost
895 boreholes along the Qinghai-Tibetan Highway in the North East of the QTP (Wu and Zhang, 2008).
896 Zhang et al. (2019) reported a ~~+30.13~~ °C per decade of warming of the permafrost top during winter
897 that is consistent with the trend of ~~+40.14~~ °C per decade we observe at 2 m depth (mean AL between
898 1.4 and 1.7 m in our simulations) for the months of December, January and February.

899 5.2.2. Evaporation and runoff changes

900 Our results are characterized by (i) an increase of both evaporation and runoff (Fig. [88A and 8B](#)),
901 mainly driven by an increase in precipitation (Fig. [3 bottom](#)), (ii) a runoff/(runoff+evaporation) ratio
902 exhibiting an increasing trend as a result of ground warming and permafrost disappearance that both
903 enable more subsurface runoff along time (Fig. [88C and 910D](#)) and (iii) an increase in the proportion
904 of liquid water in the ground compared to ice- (Fig. [8D](#)). Regarding all these points, our results find a
905 good consistency with the evolution reported by Gao et al. (2018) for the upper Heihe catchment
906 (northeastern QTP) using a similar approach for a comparable period (1971-2013). The increasing
907 trends in evaporation and runoff they report for the thawing season (dominant period for both processes)
908 are comparable with the [yearlyannual](#) values we report: ~~+100~~[10.0](#) mm ~~em~~⁺[per decade](#) for evaporation
909 (our study: ~~+10~~[10.1](#) mm per [centurydecade](#)) and ~~+333~~[33.3](#) mm per [centurydecade](#) for runoff (our study:
910 ~~+484~~[8.8](#) mm per [centurydecade](#)). Similar evolutions are also reported by Wang and Gao (2022) for the
911 Qinghai Lake catchment and by Qin et al. (2017) for the YRSR (1981-2015). Regarding differences,
912 Qin et al. (2017) modeled a stronger evaporation increase (~~143~~[14.3](#) mm per [centurydecade](#)) linked to a
913 decreasing runoff coefficient. [Similarly](#) ~~Similar~~ to Li et al. (2019), we see that an important part of snow
914 melt (49%) infiltrates ~~in~~ the ground and later contributes to runoff and evaporation.

915 5.3. Evaporation vs runoff and sensitivity to climate conditions

916 Our results indicate that evaporation is particularly strong in the Paiku catchment. Over the 40
917 years of simulation, 10% of the total precipitation is converted to runoff, [and](#) the rest of the water is
918 either directly returned to the atmosphere from the snowpack via snow sublimation or from the ground
919 surface via evaporation. Comparatively, Gao et al. (2018) observed and modeled a ratio of around 35%
920 for the Heihe catchment; Qin et al. (2017) reported an average ratio of 33% for the YRSR and Li et al.
921 (2014) a ratio of 83% for the Qugaqie catchment (central QTP) but modeling hydrological fluxes only.

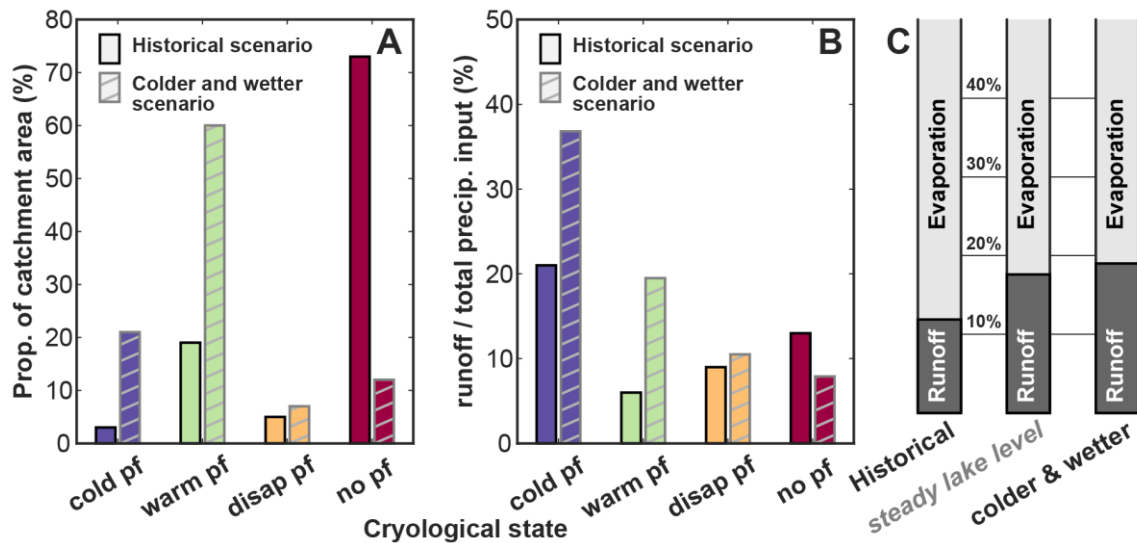
922 The role of permafrost regarding the runoff/evaporation distribution is a complex question (Bring
923 et al., 2016). Some studies have suggested that landscape-scale permafrost thaw would trigger more
924 evaporation (~~Walvoord and Kurylyk, 2016, Fig. 4~~). ([Walvoord and Kurylyk, 2016, Fig. 4 therein](#)). This
925 phenomenon was modeled by Wang et al. (2018) in the upper Heihe River Catchment, for which they

926 reported that the thickening of the active layer increased the ground storage capacity and led to a
927 decrease in runoff and an increase in evapotranspiration. Studying evaporation at the scale of the whole
928 Tibetan plateau, Wang et al. (2020b) also reported that permafrost thawing accelerated
929 evapotranspiration (1961-2014).

930 Conversely, Zhang et al. (2003) and Carey and Woo, (1999) reported that shallow frozen ground
931 conditions (such as a shallow active layer) maintain higher water contents close to the surface,
932 promoting higher evaporation. Sjöberg et al. (2021) modeled this phenomenon with a fully coupled
933 cryo-hydrological model including surface energy balance calculation. They modeled a slope with a
934 simplified geometry in 2D for different permafrost coverages. They found that hillslopes with
935 continuous permafrost have twice as high rates of evapotranspiration compared to hillslopes with no
936 permafrost.

937 As such, the interplay between the runoff/evaporation distribution and the ground thermal regime
938 in areas where permafrost coverage shows a spatiotemporal variability is difficult to apprehend. This
939 complexity is most likely due to a strong sensitivity to the drainage conditions (fast flows of steep
940 mountain environments vs. slow flows of lowland catchments) and to the climate setting, both at the
941 annual scale (arid regions vs. wet regions) and at the seasonal time scale (relative timing of temperature
942 variations, rainfall, snowfall, snow melt and ground freeze/thaw).

943 To further understand this question in the case of the Paiku catchment, we conducted a simple
944 sensitivity test on the climatic conditions. We ran the same 40 years of simulations (with thermal
945 initialization) for a climate 1 °C cooler and 30% wetter (more precipitation) than the historical scenario.
946 We call this new scenario *colder and wetter* (to be compared with the *historical scenario*, i.e. the results
947 of the present study presented in Sect. 4). Results of this experiment are presented in Fig. [4011](#). Because
948 of the difference in climate forcing, the *colder and wetter* scenario produced a greater amount of *cold*
949 and *warm permafrost* areas than the historical scenario, as presented on Fig. [40A11A](#). Fig. [40B11B](#)
950 shows the proportion of the precipitation reaching the surface (rain + snow – snow sublimation) that
951 produces runoff compared to evaporation for the Paiku catchment.



952
 953 *Figure 10.11. Sensitivity of the distribution between runoff and evaporation to climate. A: distribution*
 954 *of the different cryological states of the ground for the historical scenario (presented in Section 4) and*
 955 *for an alternative scenario where the climate is 1 °C colder and brings 30% more precipitation. B:*
 956 *runoff as a proportion of the precipitation input to the land (rainfall + snowfall – snow sublimation)*
 957 *for the different cryological states of the ground and for the 2 climatic scenarios. C: catchment scale*
 958 *ratio between runoff and evaporation for (i) the historical scenario, (ii) for a steady lake level with the*
 959 *same glacier contribution (same as Fig. 8 bottom left) (8C), and (iii) for the colder and wetter scenario.*
 960

961 The *historical scenario* shows that *cold permafrost* areas ~~produces~~produce the highest proportion
 962 of runoff, which we attribute to the fact that the ground in these areas is most of the time frozen, turning
 963 a substantial part of the snow melt and rainfall into surface runoff. When considering grounds with a
 964 hydrologically active subsurface (*warm permafrost*, *disappearing permafrost* and *no permafrost*) in the
 965 historical scenario, the proportion of runoff increases slightly from *warm permafrost* to *no permafrost*.
 966 Such an evolution then corroborates the idea that the presence of permafrost tends to increase
 967 evaporation at the expense of runoff, as modeled by Sjöberg et al. (2021). Yet, for the *colder and wetter*
 968 scenario, runoff shows a regular decrease from *cold* to *no permafrost* with a more pronounced trend
 969 than the historical scenario. Several factors can be at play in this transition and most likely involve (i)
 970 a different extent and altitudinal distribution for each cryological ~~type~~type of ground, (ii) a reduced
 971 intensity of evaporation due to cooler surface temperatures, (iii) a higher soil water content driven by
 972 higher precipitation and (iv) difference in the seasonal timings as listed earlier. Altogether, these
 973 processes substantially change the proportion of water that ends up as runoff water available for the
 974 lake, as highlighted by Fig. 10.11C.

5.4. Implications for lake level changes over the QTP

At the scale of the Paiku catchment and in regard of lake level variations, the results we present highlight that:

- The sum of the direct precipitation in the lake, the land runoff and the glacier runoff are not enough to compensate the lake evaporation over the study period, hence leading to the observed lake level decrease.
- Long term hydrological trends in the catchment are led by trends in the climate, as precipitation increase both drives an evaporation and runoff increase over the 40 years.
- Ground thermal changes increase the distribution of liquid vs. frozen water in the ground and the duration of seasonal thaw, both directly affecting evaporation and runoff towards the lake.
- Ground warming and permafrost thawing promote subsurface runoff over time, contributing to increase the runoff/evaporation ratio of the catchment.
- Over the last 40 years, the presence of permafrost seems to promote evaporation at the expense of runoff. Yet this trend appears to be climate dependent and the cryological state of the ground might shift the runoff/evaporation distribution in the other direction under colder and wetter climates.

At the scale of the QTP, these results have several implications. First, a better understanding of the recent and future lake level variations will come with a better knowledge of spatial patterns and temporal trends in precipitation. Second, climate changes are modifying the ground thermal regime of Tibetan catchments through active layer deepening and changes in the seasonal freeze/thaw cycles, affecting evaporation, runoff volumes and pathways and overall, changing the hydrological functioning of Tibetan catchments (and the waterflow provided to the lakes). Finally, the effect of permafrost on the distribution between evaporation and runoff seems to be dependent on the climate settings and the permafrost coverage of the catchment. Because it can both promote evaporation or runoff depending on the setting, the ground thermal regime of the catchment seems to have the possibility to create a positive feedback, both towards lake level decrease or increase. Further studies ~~could~~ should therefore focus on comparing the thermo-hydrological regime of different Tibetan catchments with ~~contrasted~~ contrasting

1001 lake level changes and permafrost coverage, to test to which extent these differences can explain the
1002 spatial patterns of lake level changes across the QTP.

1003 6. Conclusion

1004 We confirm that the Paiku catchment presents different types of ground cryological ~~states~~ from
1005 ~~seasonal~~ seasonally frozen ground to permafrost. Permafrost coverage shrinks from 27 to 22% of the
1006 land area of the catchment from the 1980s to the 2010s (19% loss of the 1980 permafrost area). The
1007 whole catchment warms up at a rate of 1.70.17 °C per ~~century~~ decade (2 m deep), with a substantial
1008 elevation-dependent variability. This warming is concomitant with an increase in the duration of the
1009 seasonal thaw, mainly supported by a progressive delay of the end date of the thaw period. Where
1010 permafrost is present, active layer deepening is only observed where evaporation is ~~limited~~ relatively
1011 low (<150 mm yr⁻¹).

1012 Over the simulation period, we also report an increase in evaporation (~~+10~~ 10.1 mm per
1013 ~~century~~ decade), surface and subsurface runoff (~~+13~~ 1.3 and ~~+35~~ 3.5 mm per ~~century~~ decade respectively).
1014 Together, this leads towards an increase of the runoff/(runoff + evaporation) ratio of ~~+13~~ 1.2% per
1015 ~~century~~ decade. These results highlight the strong interdependence between the ground thermal and
1016 hydrological regimes and the necessity to jointly represent them to accurately quantify evaporation and
1017 runoff in this type of environment. ~~Indeed, we show that ground thermal changes increase the~~
1018 ~~availability of liquid water in the ground and the duration of seasonal thaw and that both directly affect~~
1019 ~~evaporation and runoff towards the lake. Additionally, permafrost thawing and ground warming~~
1020 ~~promote subsurface runoff over time, contributing to increase the runoff/evaporation ratio of the~~
1021 ~~catchment.~~

1022 ~~Over~~ In regard of lake level variations, the last 40 years, results we present highlight that:

- 1023 • ~~The sum of the presence of permafrost seems to promote evaporation at the expense of runoff. Yet~~
1024 ~~this trend appears to be climate-dependent~~ direct precipitation in the lake, the land runoff and the
1025 ~~eryological state of the ground might shift the glacier runoff/~~ are not enough to compensate for the
1026 lake evaporation over the study period, hence driving the observed lake level decrease.

1027 • Long-term hydrological trends in the catchment are led by trends in climate; and precipitation
1028 increase, jointly with glacier melt, provides enough water to drive a concomitant increase of runoff
1029 and evaporation.

1030 • Ground thermal changes increase the distribution of liquid vs. frozen water in the ground and the
1031 duration of seasonal thaw, correlations suggest that these modifications increase evaporation. The
1032 warming of the ground is also related to the increase of subsurface runoff towards the lake.

1033 • Ground warming and permafrost thawing promote subsurface runoff over time, contributing to an
1034 increase in the runoff/evaporation ratio of the catchment.

1035 • Over the last 40 years, the presence of permafrost seems to promote evaporation at the expense of
1036 runoff. Yet this trend appears to be climate-dependent and the cryological state of the ground might
1037 shift the runoff/evaporation distribution in the other direction under colder and wetter climates.

1038 At the scale of the QTP, these results have several implications. First, a better understanding of the
1039 recent and future lake level variations will come with a better knowledge of spatial patterns and
1040 temporal trends in precipitation. Second, climate changes are modifying the ground thermal regime of
1041 Tibetan catchments through active layer deepening and changes in the seasonal freeze/thaw cycles,
1042 affecting evaporation, runoff volumes and pathways and overall, changing the hydrological functioning
1043 of Tibetan catchments (and the waterflow provided to the lakes). Finally, the effect of permafrost on
1044 the distribution between evaporation and runoff seems to be dependent on the climate settings and the
1045 permafrost coverage of the catchment. ~~–distribution in the other direction under colder and wetter~~
1046 ~~elimates.~~ Further studies should investigate this phenomenon and how it might contribute to
1047 ~~explain~~ explaining the ~~contrasted~~ contrasting lake level evolutions across the QTP.

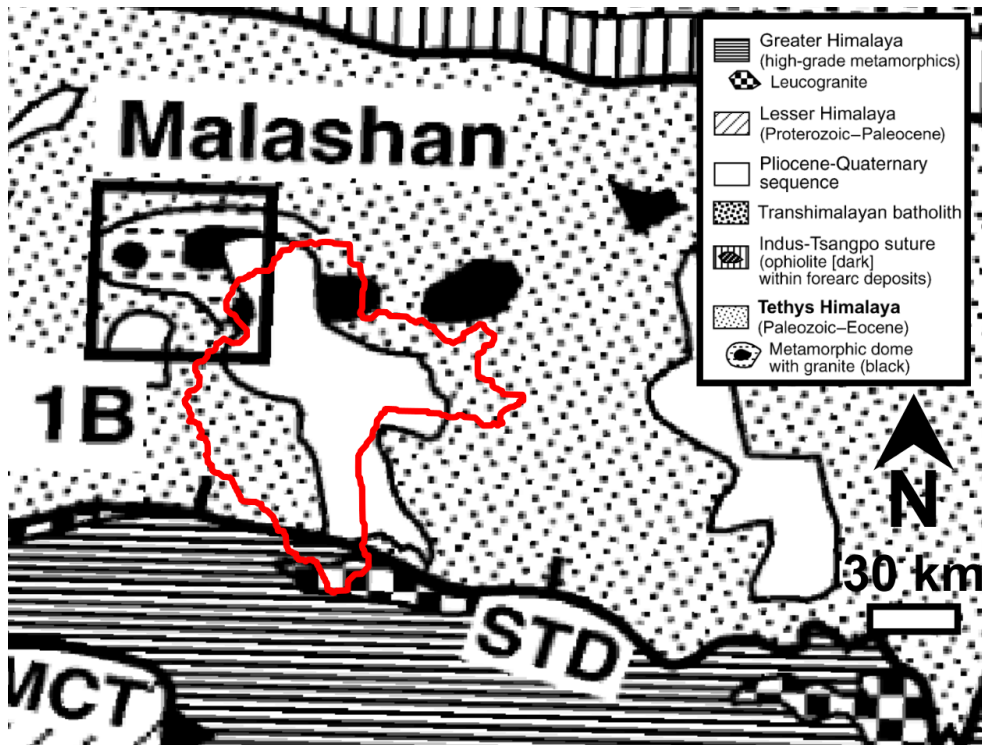
1048 **Appendix A: model parameters**

1049 *Table A.1. Parameters of the model.*

Depth	Layer	Parameter	Values	Source	Calculation
0.0 m	Surface	Albedo	0.24	Modis MCD43A3.006	November mean, 4600-5100 masl
		Emissivity	0.95	Modis MCD43A3.006	November mean, 4600-5100 masl
		Roughness	0.024	-	Adjusted to fit loggers T values
0.0 m		Thickness	0.30 m	HiHydro Soil v1.0	modeling framework
		Porosity	0.5	Shangguann et al. 2013	mean
		Organic	8.60%	HiHydro Soil v1.0	catchment mean
0.3 m	Top soil	Mineral	41.40%	-	subtraction (100 - porosity - orga)
		Soil type	Sand	Shangguann et al. 2013	dominant fraction
		Field capacity	0.32	HiHydro Soil v1.0	catchment mean
0.3 m		Hydro cond	0.000030 m s ⁻¹	HiHydro Soil v1.0	catchment mean
		Alpha	0.028 cm ⁻¹	HiHydro Soil v1.0	catchment mean
		n	1.481	HiHydro Soil v1.0	catchment mean
0.3 m		Thickness	1.70 m	Shangguan et al. 2017	truncation, consistent with litterature
		Porosity	0.4	Shangguann et al. 2013	catchment mean
		Organic	4.20%	HiHydro Soil v1.0	catchment mean
1.7 m	Bottom soil	Mineral	55.80%	-	subtraction (100 - porosity - orga)
		Soil type	Sand	Shangguann et al. 2013	dominant fraction
		Field capacity	0.32	HiHydro Soil v1.0	catchment mean
2.0 m		Hydro cond	0.000016 m s ⁻¹	HiHydro Soil v1.0	catchment mean
		Alpha	0.062 cm ⁻¹	HiHydro Soil v1.0	catchment mean
		n	1.707	HiHydro Soil v1.0	catchment mean
2.0 m		Thickness	98.3 m	-	-
		Porosity	0.03	-	-
98 m	Bedrock	Organic	0%	-	-
		Mineral	97%	-	-
100 m		Soil type	Sand	-	-
		Field Capacity	0.03	-	equal to porosity

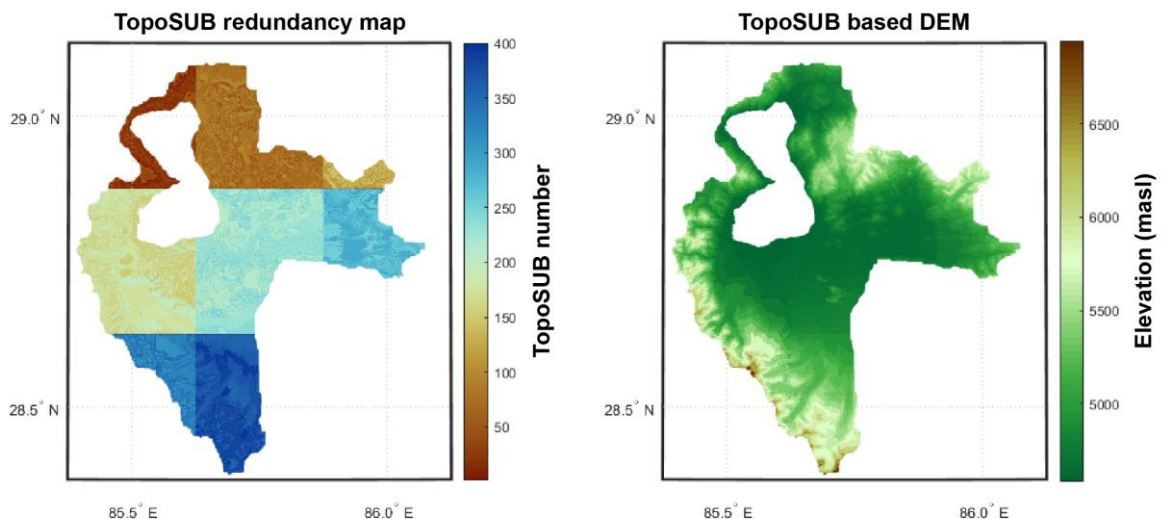
1050

1051 **Appendix B: Geological map of the catchment**



1052
1053 *Figure BB0. Geology of the catchment. Modified from Aoya et al. (2015). The red contour indicates the*
1054 *limits of the Paiku catchment.*

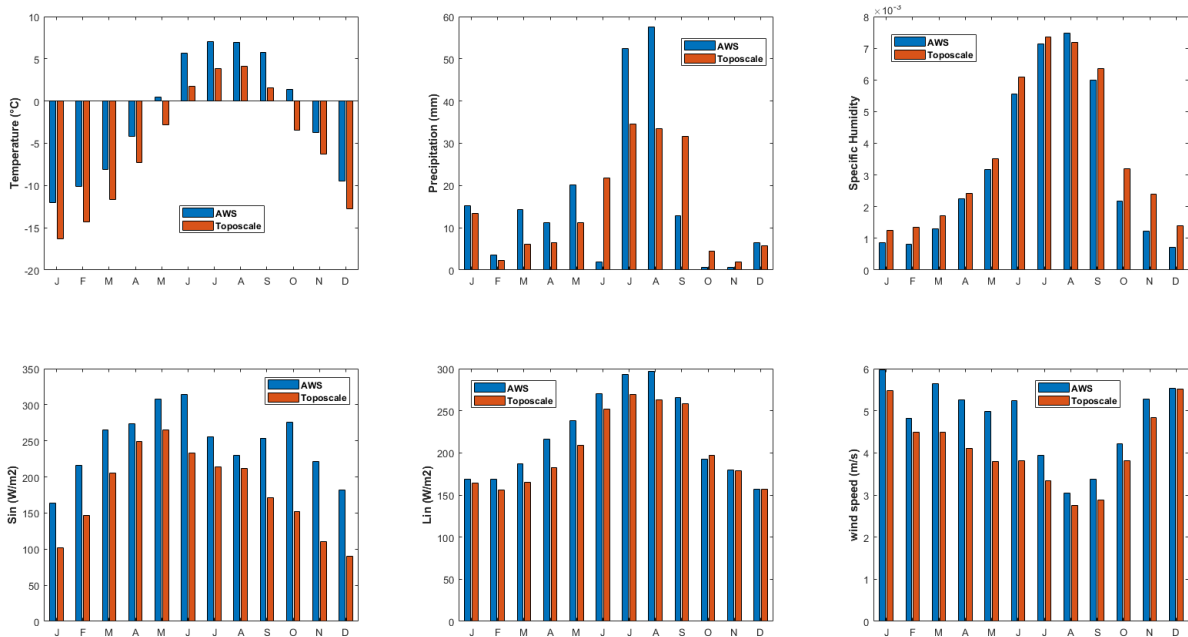
1055 **Appendix C: TopoSUB subsampling of the catchment**



1056
1057 *Figure CC0. Application of the TopoSUB clustering method (Fiddes and Gruber, 2012) in the Paiku*
1058 *catchment. Left: number of the TopoSUB points. Strong color changes reflect the footprint of the 8*
1059 *ERA5 pixels that the catchment intersects. Small color changes within a given of these zones show the*
1060 *distribution of the 50 TopoSUB points covering each tile (Sect. 3.2.2.) B: topographic map*
1061 *reconstructed from using the TopoSUB approach.*

1062

Appendix D: Evaluation of forcing data



1063

1064

1065

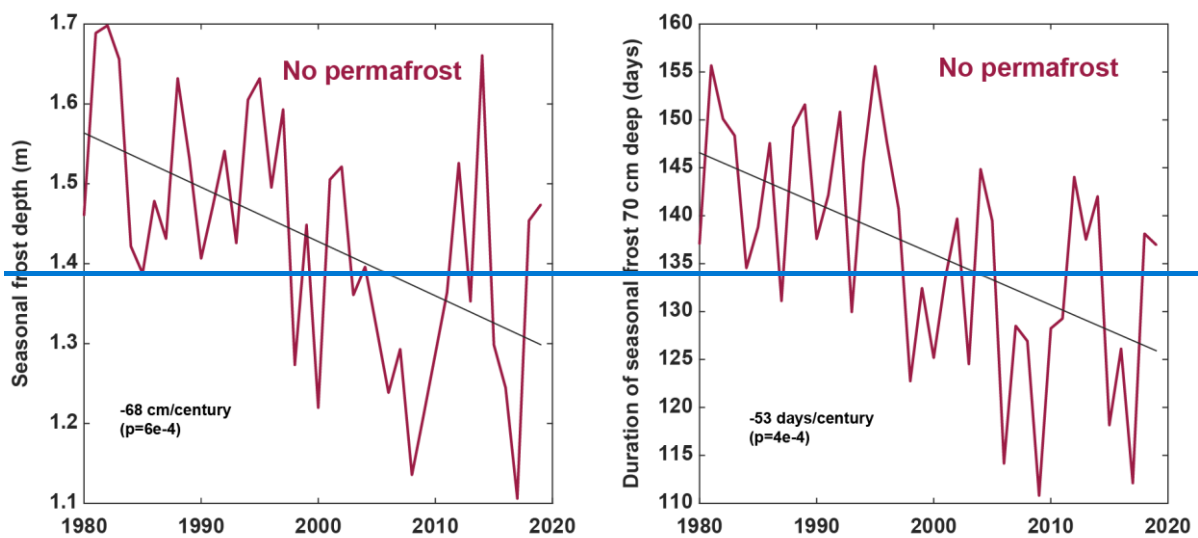
1066

1067

Figure D. Comparison between the AWS data and the model forcing data downscaled from ERA5 with the TopoSCALE and TopoSUB approaches. Based on the AWS data, a monthly correction factor is applied to the downscaled data so that monthly data matches for the observed period for each variable (methodological details in Sect. 3.2.2.).

1068

Appendix E: Seasonal frozen ground



1069

1070

1071

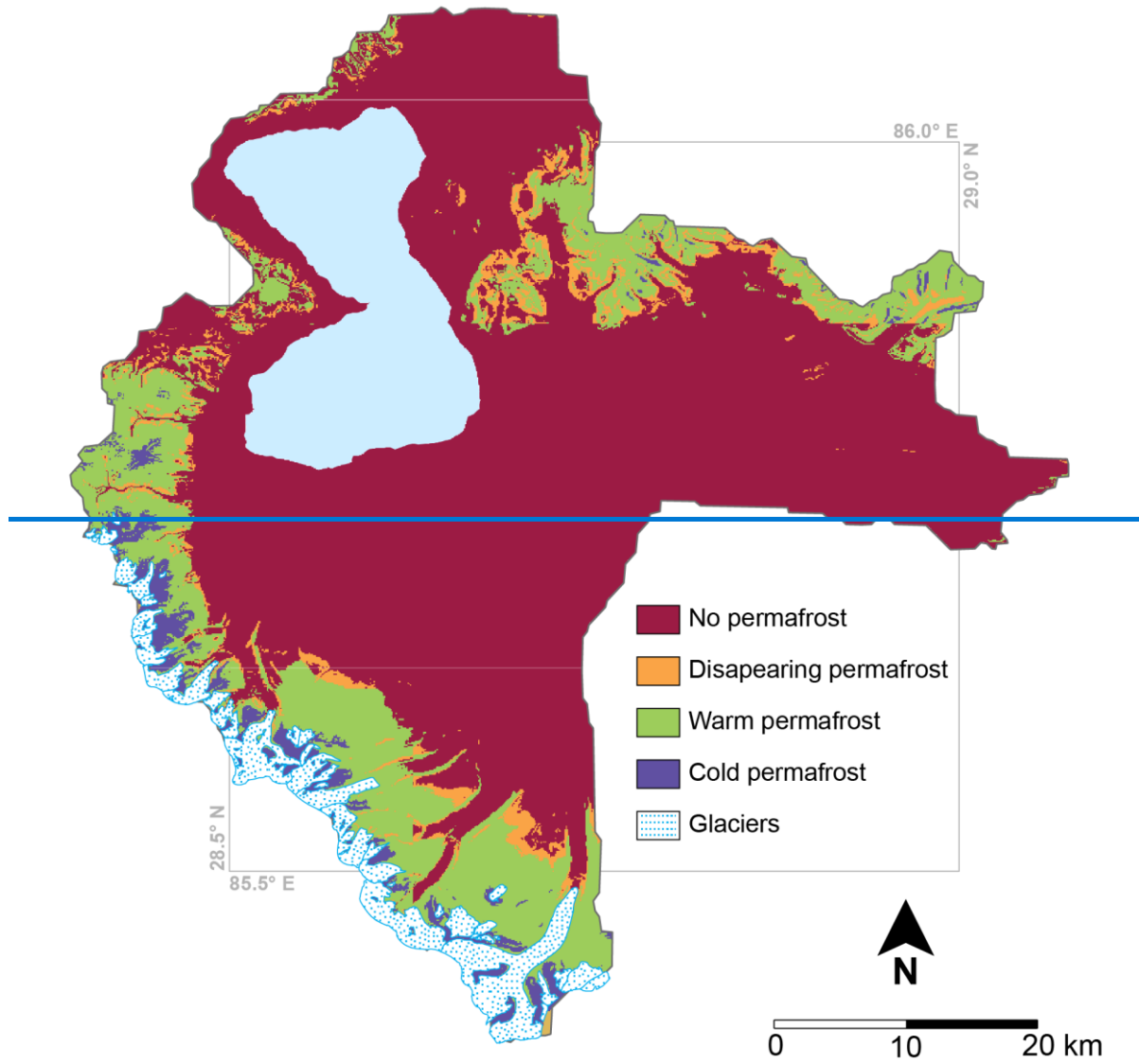
1072

1073

Figure E. Temporal trends for seasonal frozen ground where there is no permafrost. Simulations presenting occurrences of persisting thawed conditions from one year to another were excluded. The presented curves average thus 88% of the total permafrost free areas of the catchment.

1074

Appendix F: Cryological state of the ground



1075
1076

Figure F. Cryological state of the ground. See methodological descriptions in Sect. 4.2.

Code availability. The CryoGrid community model (version 1.0) and related documentation are available at: https://github.com/CryoGrid/CryoGridCommunity_source.

Data availability. Field data [have been saved on Zenodo.org and](#) will be ~~permanently deposited on~~ [XXXpublished with a DOI](#) upon acceptance of the manuscript.

Author contribution. L.M, W. I. and S.W. designed the study. L.M. and M.M. conducted the numerical simulations. S.W., M.L. and L.M. contributed to the model development. F.B., W.I., Y.L. ad S.A. acquired field data. L.M., F.B., M.M., P.K., Y.L. and T.M. analyzed and processed the data. J.F. provided downscaled forcing data for the model. All authors contributed to result interpretation and to manuscript preparation.

Competing interests. The authors declare that they have no conflict of interest.

Acknowledgements. This study was funded by the open program of the Dutch Research Council (NWO) (ALWOP.467) and by the Strategic Priority Research Program of the Chinese Academy of Sciences within the Pan-Third Pole Environment framework (grant agreement no. XDA20100300). The land surface and lake simulations were performed on Utrecht Geosciences computer cluster. Sebastian Westermann acknowledges funding by European Space Agency Permafrost_CCI (<https://climate.esa.int/en/projects/permafrost/>), (<https://climate.esa.int/en/projects/permafrost/>). We are very grateful to the reviewers for their input which significantly improved this manuscript.

References

- Aoya, M., Wallis, S. R., Terada, K., Lee, J., Kawakami, T., Wang, Y. and Heizler, M.: North-south extension in the Tibetan crust triggered by granite emplacement, *Geology*, 33(11), 853, doi:10.1130/G21806.1, 2005.
- Bhattacharya, A., Bolch, T., Mukherjee, K., King, O., Menounos, B., Kapitsa, V., Neckel, N., Yang, W. and Yao, T.: High Mountain Asian glacier response to climate revealed by multi-temporal satellite observations since the 1960s, *Nat. Commun.*, 12(1), 4133, doi:10.1038/s41467-021-24180-y, 2021.
- Bibi, S., Wang, L., Li, X., Zhou, J., Chen, D. and Yao, T.: Climatic and associated cryospheric, biospheric, and hydrological changes on the Tibetan Plateau: a review, *Int. J. Climatol.*, 38(January), e1–e17, doi:10.1002/joc.5411, 2018.
- [Biskop, S., Maussion, F., Krause, P. and Fink, M.: Differences in the water-balance components of four lakes in the southern-central Tibetan Plateau, *Hydrol. Earth Syst. Sci.*, 20\(1\), 209–225, doi:10.5194/hess-20-209-2016, 2016.](#)
- Bolch, T., Shea, J. M., Liu, S., Azam, F. M., Gao, Y., Gruber, S., Immerzeel, W. W., Kulkarni, A., Li, H., Tahir, A. A., Zhang, G. and Zhang, Y.: Status and Change of the Cryosphere in the Extended Hindu Kush Himalaya Region, in *The Hindu Kush Himalaya Assessment: Mountains, Climate Change, Sustainability and People*, edited by P. Wester, A. Mishra, A. Mukherji, and A. B. Shrestha, pp. 209–255, Springer International Publishing, Cham., 2019.
- Bring, A., Fedorova, I., Dibike, Y., Hinzman, L., Mård, J., Mernild, S. H., Prowse, T., Semanova, O., Stuefer, S. L. and Woo, M. -K.: Arctic terrestrial hydrology: A synthesis of processes, regional effects, and research challenges, *J. Geophys. Res. Biogeosciences*, 121(3), 621–649, doi:10.1002/2015JG003131, 2016.
- Brun, F., Berthier, E., Wagnon, P., Kääh, A. and Treichler, D.: A spatially resolved estimate of High Mountain Asia glacier mass balances from 2000 to 2016, *Nat. Geosci.*, 10(9), 668–673, doi:10.1038/ngeo2999, 2017.
- Brun, F., Treichler, D., Shean, D. and Immerzeel, W. W.: Limited Contribution of Glacier Mass Loss to the Recent Increase in Tibetan Plateau Lake Volume, *Front. Earth Sci.*, 8(November), 1–14, doi:10.3389/feart.2020.582060, 2020.
- Cao, J., Qin, D., Kang, E. and Li, Y.: River discharge changes in the Qinghai-Tibet Plateau, *Chinese Sci. Bull.*, 51(5), 594–600, doi:10.1007/s11434-006-0594-6, 2006.
- Carey, S. K. and Woo, M.-K.: Hydrology of two slopes in subarctic Yukon, Canada, *Hydrol. Process.*, 13(16), 2549–2562, doi:10.1002/(SICI)1099-1085(199911)13:16<2549::AID-HYP938>3.0.CO;2-H, 1999.
- Carey, S. K. and Woo, M.: Spatial variability of hillslope water balance, wolf creek basin, subarctic yukon, *Hydrol. Process.*, 15(16), 3113–3132, doi:10.1002/hyp.319, 2001.
- Chen, R., Wang, G., Yang, Y., Liu, J., Han, C., Song, Y., Liu, Z. and Kang, E.: Effects of Cryospheric Change on Alpine Hydrology: Combining a Model With Observations in the Upper Reaches of the Hei River, China, *J. Geophys. Res. Atmos.*, 123(7), 3414–3442, doi:10.1002/2017JD027876, 2018.
- Cheng, G. and Jin, H.: Permafrost and groundwater on the Qinghai-Tibet Plateau and in northeast China, *Hydrogeol. J.*, 21(1), 5–23, doi:10.1007/s10040-012-0927-2, 2013.
- [Chiasson Poirier, G., Franssen, J., Lafrenière, M. J., Fortier, D. and Lamoureux, S. F.: Seasonal evolution of active layer thaw depth and hillslope stream connectivity in a permafrost watershed, *Water Resour. Res.*, 56\(1\), 1–18, doi:10.1029/2019WR025828, 2020.](#)
- Cuo, L., Zhang, Y., Bohn, T. J., Zhao, L., Li, J., Liu, Q. and Zhou, B.: Frozen soil degradation and its effects on surface hydrology in the northern Tibetan Plateau, *J. Geophys. Res. Atmos.*, 120(16), 8276–8298, doi:10.1002/2015JD023193, 2015.
- Dall’Amico, M., Endrizzi, S., Gruber, S. and Rigon, R.: A robust and energy-conserving model of freezing variably-saturated soil, *Cryosph.*, 5(2), 469–484, doi:10.5194/tc-5-469-2011, 2011.
- Ding, Y., Zhang, S., Chen, R., Han, T., Han, H., Wu, J., Li, X., Zhao, Q., Shangguan, D., Yang, Y., Liu, J., Wang, S., Qin, J. and Chang, Y.: Hydrological Basis and Discipline System of Cryohydrology: From a Perspective of Cryospheric Science, *Front. Earth Sci.*, 8(December), 1–12, doi:10.3389/feart.2020.574707, 2020.
- Fiddes, J. and Gruber, S.: TopoSUB: A tool for efficient large area numerical modelling in complex topography at sub-grid scales, *Geosci. Model Dev.*, 5(5), 1245–1257, doi:10.5194/gmd-5-1245-2012, 2012.

- Fiddes, J. and Gruber, S.: TopoSCALE v.1.0: downscaling gridded climate data in complex terrain, *Geosci. Model Dev.*, 7(1), 387–405, doi:10.5194/gmd-7-387-2014, 2014.
- Fisher, J. P., Estop-Aragonés, C., Thierry, A., Charman, D. J., Wolfe, S. A., Hartley, I. P., Murton, J. B., Williams, M. and Phoenix, G. K.: The influence of vegetation and soil characteristics on active-layer thickness of permafrost soils in boreal forest, *Glob. Chang. Biol.*, 22(9), 3127–3140, doi:10.1111/gcb.13248, 2016.
- Gao, B., Yang, D., Qin, Y., Wang, Y., Li, H., Zhang, Y. and Zhang, T.: Change in frozen soils and its effect on regional hydrology, upper Heihe basin, northeastern Qinghai-Tibetan Plateau, *Cryosphere*, 12(2), 657–673, doi:10.5194/tc-12-657-2018, 2018.
- Gao, H., [Hrachowitz, M., Fenicia, F., Gharari, S. and Savenije, H. H. G.: Testing the realism of a topography-driven model \(FLEX-Topo\) in the nested catchments of the Upper Heihe, China, *Hydrol. Earth Syst. Sci.*, 18\(5\), 1895–1915, doi:10.5194/hess-18-1895-2014, 2014.](#)
- [Gao, H., Wang, J., Yang, Y., Pan, X., Ding, Y. and Duan, Z.: Permafrost Hydrology of the Qinghai-Tibet Plateau: A Review of Processes and Modeling, *Front. Earth Sci.*, 8\(January\), 1–13, doi:10.3389/feart.2020.576838, 2021.](#)
- [Gao, H., Han, C., Chen, R., Feng, Z., Wang, K., Fenicia, F. and Savenije, H.: Frozen soil hydrological modeling for a mountainous catchment northeast of the Qinghai–Tibet Plateau, *Hydrol. Earth Syst. Sci.*, 26\(15\), 4187–4208, doi:10.5194/hess-26-4187-2022, 2022.](#)
- van Genuchten, M. T.: A Closed-form Equation for Predicting the Hydraulic Conductivity of Unsaturated Soils, *Soil Sci. Soc. Am. J.*, 44(5), 892–898, doi:10.2136/sssaj1980.03615995004400050002x, 1980.
- Hersbach, H., Bell, B., Berrisford, P., Hirahara, S., Horányi, A., Muñoz-Sabater, J., Nicolas, J., Peubey, C., Radu, R., Schepers, D., Simmons, A., Soci, C., Abdalla, S., Abellan, X., Balsamo, G., Bechtold, P., Biavati, G., Bidlot, J., Bonavita, M., Chiara, G., Dahlgren, P., Dee, D., Diamantakis, M., Dragani, R., Flemming, J., Forbes, R., Fuentes, M., Geer, A., Haimberger, L., Healy, S., Hogan, R. J., Hólm, E., Janisková, M., Keeley, S., Laloyaux, P., Lopez, P., Lupu, C., Radnoti, G., Rosnay, P., Rozum, I., Vamborg, F., Villaume, S. and Thépaut, J.: The ERA5 global reanalysis, *Q. J. R. Meteorol. Soc.*, 146(730), 1999–2049, doi:10.1002/qj.3803, 2020.
- Hu, G.-R., Li, X.-Y. and Yang, X.-F.: The impact of micro-topography on the interplay of critical zone architecture and hydrological processes at the hillslope scale: Integrated geophysical and hydrological experiments on the Qinghai-Tibet Plateau, *J. Hydrol.*, 583(January), 124618, doi:10.1016/j.jhydrol.2020.124618, 2020.
- Huang, K., Dai, J., Wang, G., Chang, J., Lu, Y., Song, C., Hu, Z., Ahmed, N. and Ye, R.: The impact of land surface temperatures on suprapermafrost groundwater on the central Qinghai-Tibet Plateau, *Hydrol. Process.*, 34(6), 1475–1488, doi:10.1002/hyp.13677, 2020.
- Hugonnet, R., McNabb, R., Berthier, E., Menounos, B., Nuth, C., Girod, L., Farinotti, D., Huss, M., Dussaillant, I., Brun, F. and Kääb, A.: Accelerated global glacier mass loss in the early twenty-first century, *Nature*, 592(7856), 726–731, doi:10.1038/s41586-021-03436-z, 2021.
- IPCC: IPCC Special Report on the Ocean and Cryosphere in a Changing Climate, Intergov. Panel Clim. Chang., undefined [online] Available from: <https://www.ipcc.ch/srocc/chapter/summary-for-policymakers/>, 2019.
- Jiang, H., Yang, Y., Bai, Y. and Wang, H.: Evaluation of the Total, Direct, and Diffuse Solar Radiations From the ERA5 Reanalysis Data in China, *IEEE Geosci. Remote Sens. Lett.*, 17(1), 47–51, doi:10.1109/LGRS.2019.2916410, 2020.
- Jiang, Q., Li, W., Fan, Z., He, X., Sun, W., Chen, S., Wen, J., Gao, J. and Wang, J.: Evaluation of the ERA5 reanalysis precipitation dataset over Chinese Mainland, *J. Hydrol.*, 595(September 2020), 125660, doi:10.1016/j.jhydrol.2020.125660, 2021.
- Jiao, D., Xu, N., Yang, F. and Xu, K.: Evaluation of spatial-temporal variation performance of ERA5 precipitation data in China, *Sci. Rep.*, 11(1), 17956, doi:10.1038/s41598-021-97432-y, 2021.
- King, O., Bhattacharya, A., Bhamri, R. and Bolch, T.: Glacial lakes exacerbate Himalayan glacier mass loss, *Sci. Rep.*, 9(1), 18145, doi:10.1038/s41598-019-53733-x, 2019.
- Koren, V., Schaake, J., Mitchell, K., Duan, Q.-Y., Chen, F. and Baker, J. M.: A parameterization of snowpack and frozen ground intended for NCEP weather and climate models, *J. Geophys. Res. Atmos.*, 104(D16), 19569–19585, doi:10.1029/1999JD900232, 1999.
- Kurylyk, B. L., MacQuarrie, K. T. B. and McKenzie, J. M.: Climate change impacts on groundwater and soil temperatures in cold and temperate regions: Implications, mathematical theory, and emerging simulation tools, *Earth-Science Rev.*, 138, 313–334, doi:10.1016/j.earscirev.2014.06.006, 2014.

- Lamontagne-Hallé, P., McKenzie, J. M., Kurylyk, B. L. and Zipper, S. C.: Changing groundwater discharge dynamics in permafrost regions, *Environ. Res. Lett.*, 13(8), 084017, doi:10.1088/1748-9326/aad404, 2018.
- Langer, M., Westermann, S., Boike, J., Kirillin, G., Grosse, G., Peng, S. and Krinner, G.: Rapid degradation of permafrost underneath waterbodies in tundra landscapes-Toward a representation of thermokarst in land surface models, *J. Geophys. Res. Earth Surf.*, 121(12), 2446–2470, doi:10.1002/2016JF003956, 2016.
- Lei, Y., Yao, T., Bird, B. W., Yang, K., Zhai, J. and Sheng, Y.: Coherent lake growth on the central Tibetan Plateau since the 1970s: Characterization and attribution, *J. Hydrol.*, 483, 61–67, doi:10.1016/j.jhydrol.2013.01.003, 2013.
- Lei, Y., Yang, K., Wang, B., Sheng, Y., Bird, B. W., Zhang, G. and Tian, L.: Response of inland lake dynamics over the Tibetan Plateau to climate change, *Clim. Change*, 125(2), 281–290, doi:10.1007/s10584-014-1175-3, 2014.
- Lei, Y., Yao, T., Yang, K., Bird, B. W., Tian, L., Zhang, X., Wang, W., Xiang, Y., Dai, Y., Lazhu, Zhou, J. and Wang, L.: An integrated investigation of lake storage and water level changes in the Paiku Co basin, central Himalayas, *J. Hydrol.*, 562(May), 599–608, doi:10.1016/j.jhydrol.2018.05.040, 2018.
- Lei, Y., Yao, T., Yang, K., Ma, Y. and Bird, B. W.: Contrasting hydrological and thermal intensities determine seasonal lake-level variations – a case study at Paiku Co on the southern Tibetan Plateau, *Hydrol. Earth Syst. Sci.*, 25(6), 3163–3177, doi:10.5194/hess-25-3163-2021, 2021.
- [Lei, Y., Yang, K., Immerzeel, W. W., Song, P., Bird, B. W., He, J., Zhao, H. and Li, Z.: Critical Role of Groundwater Inflow in Sustaining Lake Water Balance on the Western Tibetan Plateau, *Geophys. Res. Lett.*, 49\(20\), doi:10.1029/2022GL099268, 2022.](#)
- Li, B., Yu, Z., Liang, Z. and Acharya, K.: Hydrologic response of a high altitude glacierized basin in the central Tibetan Plateau, *Glob. Planet. Change*, 118, 69–84, doi:10.1016/j.gloplacha.2014.04.006, 2014.
- Li, H., Li, X., Yang, D., Wang, J., Gao, B., Pan, X., Zhang, Y. and Hao, X.: Tracing Snowmelt Paths in an Integrated Hydrological Model for Understanding Seasonal Snowmelt Contribution at Basin Scale, *J. Geophys. Res. Atmos.*, 124(16), 8874–8895, doi:10.1029/2019JD030760, 2019.
- Luo, D., Jin, H., Wu, Q., Bense, V. F., He, R., Ma, Q., Gao, S., Jin, X. and Lü, L.: Thermal regime of warm-dry permafrost in relation to ground surface temperature in the Source Areas of the Yangtze and Yellow rivers on the Qinghai-Tibet Plateau, SW China, *Sci. Total Environ.*, 618, 1033–1045, doi:10.1016/j.scitotenv.2017.09.083, 2018.
- Luo, D., Jin, H., Bense, V. F., Jin, X. and Li, X.: Hydrothermal processes of near-surface warm permafrost in response to strong precipitation events in the Headwater Area of the Yellow River, Tibetan Plateau, *Geoderma*, 376(May), 114531, doi:10.1016/j.geoderma.2020.114531, 2020.
- Magnin, F., Josnin, J.-Y., Ravanel, L., Pergaud, J., Pohl, B. and Deline, P.: Modelling rock wall permafrost degradation in the Mont Blanc massif from the LIA to the end of the 21st century, *Cryosph.*, 11(4), 1813–1834, doi:10.5194/tc-11-1813-2017, 2017.
- Martin, L. C. P., Nitzbon, J., Aas, K. S. S., Etzelmüller, B., Kristiansen, H. and Westermann, S.: Stability Conditions of Peat Plateaus and Palsas in Northern Norway, *J. Geophys. Res. Earth Surf.*, 124(3), 705–719, doi:10.1029/2018JF004945, 2019.
- Maurer, J. M., Schaefer, J. M., Rupper, S. and Corley, A.: Acceleration of ice loss across the Himalayas over the past 40 years, *Sci. Adv.*, 5(6), doi:10.1126/sciadv.aav7266, 2019.
- [McDonnell, J. J.: Are all runoff processes the same?, *Hydrol. Process.*, 27\(26\), 4103–4111, doi:10.1002/hyp.10076, 2013.](#)
- Monin, A. S. and Obukhov, A. M.: Basic laws of turbulent mixing in the surface layer of the atmosphere, *Contrib. Geophys. Inst. Acad. Sci. USSR*, 151, 163–187, 1954.
- Mualem, Y.: A new model for predicting the hydraulic conductivity of unsaturated porous media, *Water Resour. Res.*, 12(3), 513–522, doi:10.1029/WR012i003p00513, 1976.
- Nakano, Y. and Brown, J.: Mathematical Modeling and Validation of the Thermal Regimes in Tundra Soils, Barrow, Alaska, *Arct. Alp. Res.*, 4(1), 19, doi:10.2307/1550211, 1972.
- Niu, L., Ye, B., Li, J. and Sheng, Y.: Effect of permafrost degradation on hydrological processes in typical basins with various permafrost coverage in Western China, *Sci. China Earth Sci.*, 54(4), 615–624, doi:10.1007/s11430-010-4073-1, 2011.

- Niu, L., Ye, B., Ding, Y., Li, J., Zhang, Y., Sheng, Y. and Yue, G.: Response of hydrological processes to permafrost degradation from 1980 to 2009 in the Upper Yellow River Basin, China, *Hydrol. Res.*, 47(5), 1014–1024, doi:10.2166/nh.2016.096, 2016.
- Obu, J., Westermann, S., Bartsch, A., Berdnikov, N., Christiansen, H. H., Dashtseren, A., Delaloye, R., Elberling, B., Etzelmüller, B., Kholodov, A., Khomutov, A., Kääh, A., Leibman, M. O., Lewkowicz, A. G., Panda, S. K., Romanovsky, V., Way, R. G., Westergaard-Nielsen, A., Wu, T., Yamkhin, J. and Zou, D.: Northern Hemisphere permafrost map based on TTOP modelling for 2000–2016 at 1 km² scale, *Earth-Science Rev.*, 193(October 2018), 299–316, doi:10.1016/j.earscirev.2019.04.023, 2019.
- Orsolini, Y., Wegmann, M., Dutra, E., Liu, B., Balsamo, G., Yang, K., de Rosnay, P., Zhu, C., Wang, W., Senan, R. and Arduini, G.: Evaluation of snow depth and snow cover over the Tibetan Plateau in global reanalyses using in situ and satellite remote sensing observations, *Cryosph.*, 13(8), 2221–2239, doi:10.5194/tc-13-2221-2019, 2019.
- [Penman, H. L.: Natural evaporation from open water, bare soil and grass, *Proc. R. Soc. London. Ser. A. Math. Phys. Sci.*, 193\(1032\), 120–145, 1948.](#)
- Pepin, N., Bradley, R. S., Diaz, H. F., Baraer, M., Caceres, E. B., Forsythe, N., Fowler, H., Greenwood, G., Hashmi, M. Z., Liu, X. D., Miller, J. R., Ning, L., Ohmura, A., Palazzi, E., Rangwala, I., Schöner, W., Severskiy, I., Shahgedanova, M., Wang, M. B., Williamson, S. N. and Yang, D. Q.: Elevation-dependent warming in mountain regions of the world, *Nat. Clim. Chang.*, 5(5), 424–430, doi:10.1038/nclimate2563, 2015.
- Pomeroy, J. W., Gray, D. M., Brown, T., Hedstrom, N. R., Quinton, W. L., Granger, R. J. and Carey, S. K.: The cold regions hydrological model: a platform for basing process representation and model structure on physical evidence, *Hydrol. Process.*, 21(19), 2650–2667, doi:10.1002/hyp.6787, 2007.
- Qiao, B., Zhu, L. and Yang, R.: Temporal-spatial differences in lake water storage changes and their links to climate change throughout the Tibetan Plateau, *Remote Sens. Environ.*, 222(December 2018), 232–243, doi:10.1016/j.rse.2018.12.037, 2019.
- Qin, Y., Yang, D., Gao, B., Wang, T., Chen, J., Chen, Y., Wang, Y. and Zheng, G.: Impacts of climate warming on the frozen ground and eco-hydrology in the Yellow River source region, China, *Sci. Total Environ.*, 605–606, 830–841, doi:10.1016/j.scitotenv.2017.06.188, 2017.
- Qin, Y., Chen, J., Yang, D. and Wang, T.: Estimating Seasonally Frozen Ground Depth From Historical Climate Data and Site Measurements Using a Bayesian Model, *Water Resour. Res.*, 54(7), 4361–4375, doi:10.1029/2017WR022185, 2018.
- Qin, Y., Wu, T., Zhang, P., Liu, W., Xue, S. and Guo, Z.: Spatiotemporal freeze–thaw variations over the Qinghai–Tibet Plateau 1981–2017 from reanalysis, *Int. J. Climatol.*, 41(2), 1438–1454, doi:10.1002/joc.6849, 2021.
- Ran, Y., Li, X. and Cheng, G.: Climate warming over the past half century has led to thermal degradation of permafrost on the Qinghai–Tibet Plateau, *Cryosph.*, 12(2), 595–608, doi:10.5194/tc-12-595-2018, 2018.
- Richards, L. A.: CAPILLARY CONDUCTION OF LIQUIDS THROUGH POROUS MEDIUMS, *Physics (College Park. Md.)*, 1(5), 318–333, doi:10.1063/1.1745010, 1931.
- Richardson, L. F.: *Weather Prediction by Numerical Process*, Cambridge University Press., 1922.
- [Schaaf, C. and Wang, Z.: MCD43A3 MODIS/Terra+ Aqua BRDF/Albedo Daily L3 Global—500 m V006, NASA EOSDIS L. Process. DAAC, 10, 2015.](#)
- [Rosenberry, D. O., Lewandowski, J., Meinikmann, K. and Nützmänn, G.: Groundwater - the disregarded component in lake water and nutrient budgets. Part 1: effects of groundwater on hydrology, *Hydrol. Process.*, 29\(13\), 2895–2921, doi:10.1002/hyp.10403, 2015.](#)
- Searle, M. P., Parrish, R. R., Hodges, K. V., Hurford, A., Ayres, M. W. and Whitehouse, M. J.: Shisha Pangma Leucogranite, South Tibetan Himalaya: Field Relations, Geochemistry, Age, Origin, and Emplacement, *J. Geol.*, 105(3), 295–318, doi:10.1086/515924, 1997.
- [Seibert, J., Rodhe, A. and Bishop, K.: Simulating interactions between saturated and unsaturated storage in a conceptual runoff model, *Hydrol. Process.*, 17\(2\), 379–390, doi:10.1002/hyp.1130, 2003.](#)
- Shangguan, W., Dai, Y., Liu, B., Zhu, A., Duan, Q., Wu, L., Ji, D., Ye, A., Yuan, H., Zhang, Q., Chen, D., Chen, M., Chu, J., Dou, Y., Guo, J., Li, H., Li, J., Liang, L., Liang, X., Liu, H., Liu, S., Miao, C. and Zhang, Y.: A China data set of soil properties for land surface modeling, *J. Adv. Model. Earth Syst.*, 5(2), 212–224, doi:10.1002/jame.20026, 2013.

- Shangguan, W., Hengl, T., Mendes de Jesus, J., Yuan, H. and Dai, Y.: Mapping the global depth to bedrock for land surface modeling, *J. Adv. Model. Earth Syst.*, 9(1), 65–88, doi:10.1002/2016MS000686, 2017.
- Shean, D. E., Bhushan, S., Montesano, P., Rounce, D. R., Arendt, A. and Osmanoglu, B.: A Systematic, Regional Assessment of High Mountain Asia Glacier Mass Balance, *Front. Earth Sci.*, 7(January), 1–19, doi:10.3389/feart.2019.00363, 2020.
- [Simons, G. W. H., Koster, R. and Droogers, P.: HiHydroSoil v2.0—A high resolution soil map of global hydraulic properties, Wageningen, The Netherlands. \[online\] Available from: \[https://www.futurewater.nl/wp-content/uploads/2020/10/HiHydroSoil_v2.0_High-Resolution_Soil_Maps_of_Global_Hydraulic_Properties.pdf\]\(https://www.futurewater.nl/wp-content/uploads/2020/10/HiHydroSoil_v2.0_High-Resolution_Soil_Maps_of_Global_Hydraulic_Properties.pdf\), 2020.](https://www.futurewater.nl/wp-content/uploads/2020/10/HiHydroSoil_v2.0_High-Resolution_Soil_Maps_of_Global_Hydraulic_Properties.pdf)
- Sjöberg, Y., Jan, A., Painter, S. L., Coon, E. T., Carey, M. P., O'Donnell, J. A. and Koch, J. C.: Permafrost Promotes Shallow Groundwater Flow and Warmer Headwater Streams, *Water Resour. Res.*, 57(2), 1–20, doi:10.1029/2020WR027463, 2021.
- Song, L., Wang, L., Li, X., Zhou, J., Luo, D., Jin, H., Qi, J., Zeng, T. and Yin, Y.: Improving Permafrost Physics in a Distributed Cryosphere-Hydrology Model and Its Evaluations at the Upper Yellow River Basin, *J. Geophys. Res. Atmos.*, 125(18), 1–22, doi:10.1029/2020JD032916, 2020.
- [Themeßl, M. J., Gobiet, A. and Leuprecht, A.: Empirical-statistical downscaling and error correction of daily precipitation from regional climate models, *Int. J. Climatol.*, 31\(10\), 1530–1544, doi:10.1002/joc.2168, 2011.](https://doi.org/10.1002/joc.2168)
- Vionnet, V., Brun, E., Morin, S., Boone, A., Faroux, S., Le Moigne, P., Martin, E. and Willemet, J.-M.: The detailed snowpack scheme Crocus and its implementation in SURFEX v7.2, *Geosci. Model Dev.*, 5(3), 773–791, doi:10.5194/gmd-5-773-2012, 2012.
- Walvoord, M. A. and Kurylyk, B. L.: Hydrologic Impacts of Thawing Permafrost—A Review, *Vadose Zo. J.*, 15(6), 0, doi:10.2136/vzj2016.01.0010, 2016.
- Wang, C., Zhao, W. and Cui, Y.: Changes in the Seasonally Frozen Ground Over the Eastern Qinghai-Tibet Plateau in the Past 60 Years Characteristics of Seasonally Frozen, , 8(July), 1–11, doi:10.3389/feart.2020.00270, 2020a.
- Wang, G., Li, Y., Hu, H. and Wang, Y.: Synergistic effect of vegetation and air temperature changes on soil water content in alpine frost meadow soil in the permafrost region of Qinghai-Tibet, *Hydrol. Process.*, 22(17), 3310–3320, doi:10.1002/hyp.6913, 2008.
- Wang, G., Lin, S., Hu, Z., Lu, Y., Sun, X. and Huang, K.: Improving Actual Evapotranspiration Estimation Integrating Energy Consumption for Ice Phase Change Across the Tibetan Plateau, *J. Geophys. Res. Atmos.*, 125(3), 1–13, doi:10.1029/2019JD031799, 2020b.
- Wang, L., Yi, C., Xu, X., Schütt, B., Liu, K. and Zhou, L.: Soil properties in two soil profiles from terraces of the Nam Co Lake in Tibet, China, *J. Mt. Sci.*, 6(4), 354–361, doi:10.1007/s11629-009-1017-3, 2009.
- Wang, Q., Fan, X. and Wang, M.: Recent warming amplification over high elevation regions across the globe, *Clim. Dyn.*, 43(1–2), 87–101, doi:10.1007/s00382-013-1889-3, 2014.
- Wang, X. and Gao, B.: Frozen soil change and its impact on hydrological processes in the Qinghai Lake Basin, the Qinghai-Tibetan Plateau, China, *J. Hydrol. Reg. Stud.*, 39(January), 100993, doi:10.1016/j.ejrh.2022.100993, 2022.
- Wang, Y., Yang, H., Gao, B., Wang, T., Qin, Y. and Yang, D.: Frozen ground degradation may reduce future runoff in the headwaters of an inland river on the northeastern Tibetan Plateau, *J. Hydrol.*, 564(May), 1153–1164, doi:10.1016/j.jhydrol.2018.07.078, 2018.
- Westermann, S., Schuler, T. V., Gislén, K. and Etzelmüller, B.: Transient thermal modeling of permafrost conditions in Southern Norway, *Cryosph.*, 7(2), 719–739, doi:10.5194/tc-7-719-2013, 2013.
- Westermann, S., Langer, M., Boike, J., Heikenfeld, M., Peter, M., Etzelmüller, B. and Krinner, G.: Simulating the thermal regime and thaw processes of ice-rich permafrost ground with the land-surface model CryoGrid 3, *Geosci. Model Dev.*, 9(2), 523–546, doi:10.5194/gmd-9-523-2016, 2016.
- Westermann, S., Ingeman-Nielsen, T., Scheer, J., Aalstad, K., Aga, J., Chaudhary, N., Etzelmüller, B., Filhol, S., Kääh, A., Renette, C., Schmidt, L. S., Schuler, T. V., Zweigel, R. B., Martin, L., Morard, S., Ben-Asher, M., Angelopoulos, M., Boike, J., Groenke, B., Miesner, F., Nitzbon, J., Overduin, P., Stuenzi, S. M. and Langer, M.: The CryoGrid community model (version 1.0) -- a multi-physics toolbox for climate-driven simulations in the terrestrial cryosphere, *Geosci. Model Dev. Discuss.*, 2022, 1–61, doi:10.5194/gmd-2022-127, 2022.
- Wu, Q. and Zhang, T.: Recent permafrost warming on the Qinghai-Tibetan Plateau, *J. Geophys. Res.*, 113(D13),

D13108, doi:10.1029/2007JD009539, 2008.

Wünnemann, B., Yan, D. and Ci, R.: Morphodynamics and lake level variations at Paiku Co, southern Tibetan Plateau, China, *Geomorphology*, 246, 489–501, doi:10.1016/j.geomorph.2015.07.007, 2015.

Yang, K., Wu, H., Qin, J., Lin, C., Tang, W. and Chen, Y.: Recent climate changes over the Tibetan Plateau and their impacts on energy and water cycle: A review, *Glob. Planet. Change*, 112, 79–91, doi:10.1016/j.gloplacha.2013.12.001, 2014a.

Yang, [K.](#), [Wang, J.](#), [Lei, Y.](#), [Chen, Y.](#), [Zhu, L.](#), [Ding, B.](#) and [Qin, J.](#): [Quantifying evaporation and its decadal change for Lake Nam Co, central Tibetan Plateau](#), *J. Geophys. Res. Atmos.*, 121(13), 7578–7591, doi:10.1002/2015JD024523, 2016.

[Yang, S.](#), [Zhang, H.](#), [Kong, M.](#), [Liu, Y.](#), [Liu, H.](#) and [Xu, R.](#): Study on surficial soil geochemistry in the high-elevation and -frigid mountainous region: A case of Qulong porphyry copper deposit in Tibet, *J. Geochemical Explor.*, 139, 144–151, doi:10.1016/j.gexplo.2013.06.001, 2014b.

Yang, Y., Wu, Q., Jin, H., Wang, Q., Huang, Y., Luo, D., Gao, S. and Jin, X.: Delineating the hydrological processes and hydraulic connectivities under permafrost degradation on Northeastern Qinghai-Tibet Plateau, China, *J. Hydrol.*, 569(November 2018), 359–372, doi:10.1016/j.jhydrol.2018.11.068, 2019.

Yao, F., Wang, J., Yang, K., Wang, C., Walter, B. A. and Crétaux, J.-F.: Lake storage variation on the endorheic Tibetan Plateau and its attribution to climate change since the new millennium, *Environ. Res. Lett.*, 13(6), 064011, doi:10.1088/1748-9326/aab5d3, 2018.

Yi, S., Arain, M. A. and Woo, M.-K.: Modifications of a land surface scheme for improved simulation of ground freeze-thaw in northern environments, *Geophys. Res. Lett.*, 33(13), L13501, doi:10.1029/2006GL026340, 2006.

Yuan, Z., Jin, H., Wang, Q., Wu, Q., Li, G., Jin, X. and Ma, Q.: Profile distributions of soil organic carbon fractions in a permafrost region of the Qinghai-Tibet Plateau, *Permafr. Periglac. Process.*, 31(4), 538–547, doi:10.1002/ppp.2055, 2020.

Zhang, G., Yao, T., Piao, S., Bolch, T., Xie, H., Chen, D., Gao, Y., O'Reilly, C. M., Shum, C. K., Yang, K., Yi, S., Lei, Y., Wang, W., He, Y., Shang, K., Yang, X. and Zhang, H.: Extensive and drastically different alpine lake changes on Asia's high plateaus during the past four decades, *Geophys. Res. Lett.*, 44(1), 252–260, doi:10.1002/2016GL072033, 2017.

Zhang, G., Nan, Z., Wu, X., Ji, H. and Zhao, S.: The Role of Winter Warming in Permafrost Change Over the Qinghai-Tibet Plateau, *Geophys. Res. Lett.*, 46(20), 11261–11269, doi:10.1029/2019GL084292, 2019.

Zhang, G., Yao, T., Xie, H., Yang, K., Zhu, L., Shum, C. K., Bolch, T., Yi, S., Allen, S., Jiang, L., Chen, W. and Ke, C.: Response of Tibetan Plateau lakes to climate change: Trends, patterns, and mechanisms, *Earth-Science Rev.*, 208(July), 103269, doi:10.1016/j.earscirev.2020.103269, 2020.

Zhang, G., Bolch, T., Chen, W. and Crétaux, J.-F.: Comprehensive estimation of lake volume changes on the Tibetan Plateau during 1976–2019 and basin-wide glacier contribution, *Sci. Total Environ.*, 772, 145463, doi:10.1016/j.scitotenv.2021.145463, 2021a.

Zhang, G., Nan, Z., Zhao, L., Liang, Y. and Cheng, G.: Qinghai-Tibet Plateau wetting reduces permafrost thermal responses to climate warming, *Earth Planet. Sci. Lett.*, 562, 116858, doi:10.1016/j.epsl.2021.116858, 2021b.

Zhang, H., Immerzeel, W. W., Zhang, F., de Kok, R. J., Chen, D. and Yan, W.: Snow cover persistence reverses the altitudinal patterns of warming above and below 5000 m on the Tibetan Plateau, *Sci. Total Environ.*, 803, 149889, doi:10.1016/j.scitotenv.2021.149889, 2022.

Zhang, Y., Ohata, T. and Kadota, T.: Land-surface hydrological processes in the permafrost region of the eastern Tibetan Plateau, *J. Hydrol.*, 283(1–4), 41–56, doi:10.1016/S0022-1694(03)00240-3, 2003.

[Zhong, X.](#), [Wang, L.](#), [Zhou, J.](#), [Li, X.](#), [Qi, J.](#), [Song, L.](#) and [Wang, Y.](#): [Precipitation Dominates Long-Term Water Storage Changes in Nam Co Lake \(Tibetan Plateau\) Accompanied by Intensified Cryosphere Melts Revealed by a Basin-Wide Hydrological Modelling](#), *Remote Sens.*, 12(12), 1926, doi:10.3390/rs12121926, 2020.

[Zhou, J.](#), [Wang, L.](#), [Zhang, Y.](#), [Guo, Y.](#), [Li, X.](#) and [Liu, W.](#): [Exploring the water storage changes in the largest lake \(Selin Co\) over the Tibetan Plateau during 2003–2012 from a basin-wide hydrological modeling](#), *Water Resour. Res.*, 51(10), 8060–8086, doi:10.1002/2014WR015846, 2015.

Zou, D., Zhao, L., Sheng, Y., Chen, J., Hu, G., Wu, T., Wu, J., Xie, C., Wu, X., Pang, Q., Wang, W., Du, E., Li, W., Liu, G., Li, J., Qin, Y., Qiao, Y., Wang, Z., Shi, J. and Cheng, G.: A new map of permafrost distribution on the Tibetan Plateau, *Cryosph.*, 11(6), 2527–2542, doi:10.5194/tc-11-2527-2017, 2017.

Zweigel, R. B., Westermann, S., Nitzbon, J., Langer, M., Boike, J., Etzelmüller, B. and Vikhamar Schuler, T.:
Simulating Snow Redistribution and its Effect on Ground Surface Temperature at a High-Arctic Site on
Svalbard, *J. Geophys. Res. Earth Surf.*, 126(3), 1–21, doi:10.1029/2020JF005673, 2021.